

NAVENVPREDRSCH  
TECHNICAL REPORT  
TR 78-04

LEVEL <sup>11</sup> (13)

USE OF A SECOND-MOMENT TURBULENCE  
CLOSURE MODEL FOR COMPUTATION OF  
REFRACTIVE INDEX STRUCTURE COEFFICIENTS

Stephen D. Burk

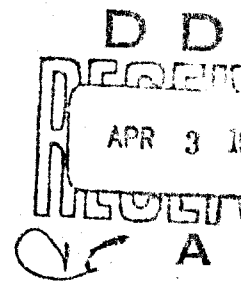
Naval Environmental Prediction Research Facility

NAVENVPREDRSCH TR 78-04

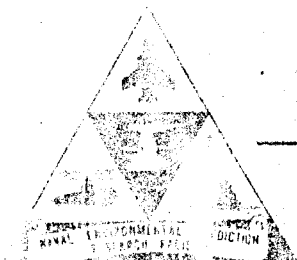
AD A0 66742

FILE COPY

DECEMBER 1978



APPROVED FOR PUBLIC RELEASE  
DISTRIBUTION UNLIMITED



NAVAL ENVIRONMENTAL PREDICTION RESEARCH FACILITY  
MONTEREY, CALIF 93940

79 04 02

BEST AVAILABLE COPY

Qualified requestors may obtain additional copies from the Defense Documentation Center. All others should apply to the National Technical Information Service.

**BEST AVAILABLE COPY**

UNCLASSIFIED

SECURITY CLASSIFICATION OF THIS PAGE (When Data Entered)

REPORT DOCUMENTATION PAGE		READ INSTRUCTIONS BEFORE COMPLETING FORM
1. REPORT NUMBER NAVENVPREDRSCHFAC Technical Report TR 78-04	2. GOVT ACCESSION NO.	3. RECIPIENT'S CATALOG NUMBER
4. TITLE (and Subtitle) Use of a Second-Moment Turbulence Closure Model for Computation of Refractive Index Structure Coefficients	5. TYPE OF REPORT & PERIOD COVERED 9 Final rept.	
7. AUTHOR(s) 10 Stephen D./Burk	8. CONTRACT OR GRANT NUMBER(s) 14 NEPRF-TR-78-04	
9. PERFORMING ORGANIZATION NAME AND ADDRESS Naval Environmental Prediction Research Facility Monterey, CA 93940	10. PROGRAM ELEMENT, PROJECT, TASK AREA & WORK UNIT NUMBERS PE 63207N, PN 7W0513 TA CC00, NEPRF WU 6.3-8	
11. CONTROLLING OFFICE NAME AND ADDRESS Naval Air Systems Command Department of the Navy Washington, DC 20361	12. REPORT DATE 11 December 1978	
14. MONITORING AGENCY NAME & ADDRESS (if different from Controlling Office) 16 W0513 17 W0513 CC00	13. NUMBER OF PAGES 62 12 60p	
15. SECURITY CLASS. (of this report) UNCLASSIFIED		15a. DECLASSIFICATION/DOWNGRADING SCHEDULE
16. DISTRIBUTION STATEMENT (of this Report) Approved for public release; distribution unlimited.		
17. DISTRIBUTION STATEMENT (of the abstract entered in Block 20, if different from Report)		
18. SUPPLEMENTARY NOTES Original manuscript received in June 1978		
19. KEY WORDS (Continue on reverse side if necessary and identify by block number) numerical modeling      refractive index marine planetary boundary layer      structure functions turbulence closure model		
20. ABSTRACT (Continue on reverse side if necessary and identify by block number) A one-dimensional second-moment turbulence closure model which includes a detailed radiative transfer scheme and a parameterized cloud physics is described. The Reynolds equations are developed from the primitive set of equations and the necessary closure assumptions are discussed. The nature of initial and boundary conditions required by the model, both for the mean and the turbulence variables, is presented.		

DD FORM 1 JAN 73 1473

EDITION OF 1 NOV 65 IS OBSOLETE  
S/N 0102-014-6601

UNCLASSIFIED

SECURITY CLASSIFICATION OF THIS PAGE (When Data Entered)

407 279

79

04

02

120

JOB

UNCLASSIFIED

SECURITY CLASSIFICATION OF THIS PAGE(When Data Entered)

20. Abstract (continued)

A discussion of acoustic, optical and microwave refractive index structure parameters,  $C_n^2$ , is then presented. The functional dependence of  $C_n^2$  on  $C_T^2$ ,  $C_e^2$  and  $C_{Te}^2$  is outlined for acoustic, optical, and microwave radiation. Model results are given for several marine boundary layer cases and one overland simulation. The first case is based upon a numerical experiment performed by Sommeria using the Deardorff 3-D subgrid scale turbulence model. Despite the use of similar initial and boundary conditions, the second-moment closure model produced some significant differences in the mean fields as compared to the 3-D model; these differences are discussed. The second case utilizes data from CEWCOM-76 to provide a test case for the model. The third experiment is an overland simulation in which the thermal driving force is a specified diurnal wave in surface temperature. In each experiment, the vertical profiles of acoustic and microwave  $C_n^2$  throughout the PBL and their dependences upon  $C_T^2$ ,  $C_e^2$  and  $C_{Te}^2$  are examined. The functional dependence of optical  $C_n^2$  is very similar to that of acoustic  $C_n^2$ , so it is not examined in extensive detail.

UNCLASSIFIED

SECURITY CLASSIFICATION OF THIS PAGE(When Data Entered)



# CONTENTS

1. INTRODUCTION . . . . .	1
2. THE MODEL . . . . .	5
2.1 Model Equations . . . . .	5
2.1.1 Derivation of Dynamic Equations for Turbulent Moments . . . . .	5
2.1.2 Closure Relationships and the Full Set of Equations . . . . .	9
2.1.3 Thermodynamic Variables and Treatment of Clouds . . . . .	13
2.1.4 Radiative Transfer . . . . .	14
2.2 Model Structure and Boundary Conditions . . . . .	15
3. REFRACTIVE INDEX STRUCTURE COEFFICIENTS . . . . .	19
4. MODEL EXPERIMENTS AND RESULTS . . . . .	23
4.1 Case A . . . . .	23
4.2 Case B . . . . .	26
4.3 Case C . . . . .	30
5. CONCLUDING REMARKS . . . . .	33
ACKNOWLEDGMENTS . . . . .	36
REFERENCES . . . . .	37
FIGURES . . . . .	41

ADDITIONAL BY	
NTIS	Whole Section <input checked="" type="checkbox"/>
DOC	Part Section <input type="checkbox"/>
UNANNOUNCED	<input type="checkbox"/>
JUSTIFICATION	
BY	
DISTRIBUTION/AVAILABILITY CODES	
Dist.	AVAIL. and/or SPECIAL
A	

## 1. INTRODUCTION

Fluctuations in atmospheric refractive index frequently are a nuisance to the engineer concerned with coherent propagation of microwave, acoustic or visible radiation. For example, images viewed through a telescope suffer a loss of resolution due to such fluctuations, which is part of the reason astronomical observatories are generally located at high elevations where the overlying air mass is reduced.

In recent years, however, refractive fluctuations have proven increasingly beneficial to the meteorologist. Because these fluctuations distort and scatter electromagnetic radiation and sound waves, they permit remote sounding of the atmospheric turbulence field. Thus the use of lasers, acoustic sounders and a variety of radars for remotely sensing the atmosphere is now common practice in many meteorological field experiments.

As Gossard (1978) has pointed out, this burgeoning use of remote sensors has created an urgent need for an understanding of how the detailed boundary layer structure affects responses of such sensors. A further beneficial outgrowth of these investigations has been an increased cooperation and collaboration among experimentalists and boundary layer turbulence theoreticians.

Within the inertial subrange of high Reynolds' number turbulence, the refractive index structure function is

$$[n(\underline{x}) - n(\underline{x}+\underline{r})]^2 = C_n^2 r^{2/3}, \quad (1)$$

where  $n$  is refractive index,  $\underline{x}$  and  $\underline{r}$  are position vectors, and  $r = |\underline{r}|$ . Here  $C_n^2$  is the refractive index structure parameter and may be regarded as an indicator of refractive index fluctuation intensity. The backscattered return to the remote sensing devices mentioned above is related to  $C_n^2$ . This report is primarily concerned with the detailed nature of the refractive index structure parameter within the planetary boundary layer (PBL).

Study of the statistical properties of structure functions within turbulent flows traces back to the pioneers of turbulence theory (e.g., Kolmogorov, 1941; Taylor, 1935). The hypothesis of local isotropy, when combined with the physical and dimensional reasoning which comprises similarity theory, permitted these theoreticians to develop general and far-reaching statements concerning the nature of turbulence. The work of Tatarskii (1961, 1971) represents a major step toward an understanding of the influence of turbulence upon wave propagation.

In a moist atmosphere, turbulent fluctuations of temperature, humidity and pressure can all contribute to variations of refractive index. However, in most circumstances the fluctuating pressure contribution is found to be negligible. The possible importance of the temperature-humidity covariance,  $\overline{T'q'}$ , to the backscatter of microwave radiation was demonstrated by Gossard (1960). In most circumstances, however, the variance of microwave refractive index is determined by the humidity variance. But the relative importance of temperature and humidity variances, and their covariance, to the refractive index variance depends upon whether one is considering optical, acoustic or microwave propagation.

For optical and acoustic waves, temperature-induced density changes have generally been considered to be the dominant source of refractive index variance. More recently, the contributions of humidity fluctuations and the humidity-temperature correlation to acoustic and optical refractive index variations have come under increased scrutiny (Wesely and Derzko, 1975; Friehe et al., 1975; Wesely, 1976). In the numerical experiments described in this report, the individual influences of temperature and humidity fluctuations upon acoustic, optical and microwave structure parameters are examined in both marine and continental boundary layer simulations.

Numerical boundary layer modeling is a remarkably fast-growing field of meteorology. The expanding collection of second-moment and subgrid-scale closure models can be bewildering to the boundary



layer specialist as well as to those in related scientific fields. The additional complexity of these models can be justified only if they can more accurately represent the physics involved. Certainly these sophisticated models are no less empirical in nature than earlier boundary layer models, and must be regarded only as one further step toward an understanding of boundary layer processes.

The additional complexity of second-moment closure models offers the benefit of additional information concerning the ensemble-average statistical properties of the turbulence field. In such closure models, not only are equations for the mean variables solved (as in the usual primitive equation model), but one also solves equations for the many Reynolds terms of momentum, heat and moisture flux. Among the interesting turbulence quantities calculated are the temperature and humidity variances, and the temperature-humidity covariance. From these turbulence variables, refractive index variance for microwave, acoustic, and optical radiation can be computed. This is the technique presented in this report.

There are restrictions on the interpretation of results derived from a second-moment closure model which must be clearly stated and recognized. The model does not deal directly with the instantaneous perturbation properties of the turbulent flow. Instead, ensemble-averaged quantities are the dependent variables. Thus, in computing a refractive index structure parameter based upon the variances of temperature and moisture, and their covariance, we are examining a  $C_n^2$  representative of ensemble-averaged statistics of the boundary layer. Wyngaard et al. (1971) note that such ensemble-averaged quantities lack the intermittent burst of activity associated with short term averages. This is the reason, for example, that vertical profiles of the temperature structure parameter,  $C_T^2$ , which are found from short time averages, often have a very jagged appearance (Fritz and Lawrence, 1977) as compared to those computed from a closure model.

Of course, the response of a remote sensing device is directly related to the short term behavior of the structure parameter rather than to its ensemble-averaged value. It is necessary to look to the longer term behavior of such short-time-averaged statistics in hopes of achieving an adequate comparison with model predictions. This situation is analogous to the position maintained by statistical mechanics, relative to classical thermodynamics. In statistical mechanics one seeks more information than simply the quasi-equilibrium values of initial and final state, but is incapable of dealing with the full complexity of the instantaneous behavior of the system. Thus, the ensemble-averaged dynamic behavior of the system is examined.

Section 2 of this report describes the origin of the equations which make up the second-moment closure model and discusses the nature of the boundary conditions used. Section 3 discusses the functional dependence of acoustic, optical and microwave structure coefficients upon temperature and moisture fluctuations. Three separate boundary layer simulations are presented and their results are discussed in Section 4. Concluding remarks are given in Section 5.



## 2. THE MODEL

### 2.1 MODEL EQUATIONS

The model is a Boussinesq, one-dimensional, second-moment, turbulence closure model. First it is necessary to demonstrate how equations describing the dynamic behavior of the second turbulence moments may be generated, and also to note the point at which such closure models depart from conventional eddy coefficient models.

#### 2.1.1 Derivation of Dynamic Equations for Turbulent Moments

Begin with the Boussinesq equations of motion; the conservation equation for a scalar property,  $S$ , and the continuity equation:

$$\begin{aligned} \frac{\partial \tilde{U}_i}{\partial t} = & - \frac{\partial}{\partial x_k} (\tilde{U}_k \tilde{U}_i) - \frac{1}{\langle \tilde{\rho} \rangle} \frac{\partial \tilde{p}}{\partial x_i} - \epsilon_{ikl} f_k \tilde{U}_l \\ & + \left[ \frac{\tilde{\theta}_v - \langle \tilde{\theta}_v \rangle}{\langle \tilde{\theta}_v \rangle} - 1 \right] \delta_{i3} g + \nu \frac{\partial^2 \tilde{U}_i}{\partial x_k \partial x_k} \end{aligned} \quad (2)$$

$$\frac{\partial \tilde{S}}{\partial t} = - \frac{\partial}{\partial x_k} (\tilde{U}_k \tilde{S}) + \gamma_s \frac{\partial^2 \tilde{S}}{\partial x_k \partial x_k} \quad (3)$$

$$\frac{\partial \tilde{U}_i}{\partial x_i} = 0. \quad (4)$$

The symbols are conventional, representing the velocity vector,  $U_i$ ; pressure,  $p$ ; density,  $\rho$ ; virtual potential temperature,  $\theta_v$ ; gravitational acceleration,  $g$ ; and  $\nu$  and  $\gamma_s$  the kinematic viscosity and molecular diffusivity for property  $S$ , respectively. The alternating tensor,  $\epsilon_{ijk}$ , is used in defining the cross product which appears in the Coriolis force term;  $f_k$  is the Coriolis parameter. For purposes of this illustration no source or sink term is included in Eq. (3). Note that the advective terms have been written in flux form by use of Eq. (4).

In order to derive equations for the time dependence of the mean variables, the Reynolds averaging convention,

$$\tilde{X}_i = X_i + x_i'; \quad \overline{x_i'} = 0,$$

is introduced, with  $X$  representing any one of the model variables. Mean variables are represented by the upper case, while perturbation quantities have a prime indicating the fluctuating departure from the mean. Inserting these decompositions into the equations of motion and then performing a Reynolds average yields the averaged equations of motion,

$$\frac{\partial U_i}{\partial t} = - \frac{\partial}{\partial x_i} [U_k U_i + \overline{u_i' u_k'}] - \frac{1}{\langle \rho \rangle} \frac{\partial p}{\partial x_i} - \epsilon_{ikl} f_k U_l \quad (5)$$

$$\left[ \frac{\langle \theta_v - \langle \theta_v \rangle \rangle}{\langle \theta_v \rangle} - 1 \right] \delta_{i3} g + \nu \frac{\partial^2 U_i}{\partial x_k \partial x_k}$$

Treating Eqs. (3) and (4) in a similar manner gives

$$\frac{\partial S}{\partial t} = - \frac{\partial}{\partial x_k} [U_k S + \overline{u_k' s'}] + \gamma_s \frac{\partial^2 S}{\partial x_k \partial x_k}, \quad (6)$$

$$\frac{\partial U_i}{\partial x_i} = 0. \quad (7)$$

The form of Eqs. (5)-(7) is quite similar to that of Eqs. (2)-(4). However, additional terms involving the momentum and scalar fluxes,  $\overline{u_i' u_k'}$  and  $\overline{u_k' s'}$ , appear in Eqs. (5) and (6). These terms owe their existence to the nonlinear advection terms rather than the molecular dissipation terms, but in spite of this they are frequently identified as "friction" terms. When attempting to integrate the full set of primitive equations, it is turbulent moments such as these that create a closure problem. That is, there are more unknowns than equations. The choice becomes one of either devising a method of reducing the number of unknowns at this stage of development, or of generating additional equations which describe the dynamic behavior of these turbulent moments. This is the point of departure of the eddy coefficient (K-theory) and the second-moment closure approaches.

Typically, K-theory relies upon mixing length arguments and analogies with molecular diffusion in order to write

$$-\overline{u_i' s'} = K_i \frac{\partial S}{\partial x_i}, \quad (8)$$

where  $K_i$  is the eddy coefficient in the  $x_i$ -direction. Thus, insertion of Eq. (8) in Eq. (6) reduces the number of unknowns provided  $K_i$  may somehow be specified. Techniques for specification of  $K_i$  have been developed for use in simple boundary layer situations (e.g., O'Brien, 1970). But, since  $K_i$  is a property of the nonlinear turbulent flow and not a fluid property, specification of  $K_i$  a priori can become a near impossibility when a variety of meteorologically complex situations are to be addressed.

The second-moment closure technique uses the second of the approaches mentioned above; namely, additional equations describing the dynamic behavior of the turbulent moments are developed. To illustrate how such moment equations are derived: subtracting the averaged Eqs. (5)-(7) from their respective equations for instantaneous variables (2)-(4), yields equations for the perturbations:

$$\begin{aligned} \frac{\partial u_i'}{\partial t} = & - \frac{\partial}{\partial x_k} [U_k u_i' + u_k' U_i + u_i' u_k' - \overline{u_i' u_k'}] - \frac{1}{\langle \rho \rangle} \frac{\partial p'}{\partial x_i} \\ & - \epsilon_{ikl} f_k' u_l' + \frac{\theta_V'}{\langle \theta_V \rangle} \delta_{i3} g + \nu \frac{\partial^2 u_i'}{\partial x_k \partial x_k}, \end{aligned} \quad (9)$$

$$\frac{\partial s'}{\partial t} = - \frac{\partial}{\partial x_k} [U_k s' + u_k' S + u_k' s' - \overline{u_k' s'}] + \gamma_s \frac{\partial^2 s'}{\partial x_k \partial x_k}, \quad (10)$$

$$\frac{\partial u_i'}{\partial x_i} = 0. \quad (11)$$

An equation for the dynamic behavior of the stresses,  $\overline{u_i' u_j'}$ , is derived by first multiplying Eq. (9) by  $u_j'$ ; then replacing subscript  $i$  with  $j$  in Eq. (9); and forming a second equation by multiplying by  $u_i'$ . Adding these two equations and performing a Reynolds average gives:



$$\begin{aligned}
\frac{\partial}{\partial t}(\overline{u_i' u_j'}) + \frac{\partial}{\partial x_k}(U_k \overline{u_i' u_j'}) = & - \overline{u_j' u_k'} \frac{\partial U_i}{\partial x_k} - \overline{u_i' u_k'} \frac{\partial U_j}{\partial x_k} - \frac{\partial}{\partial x_k}(\overline{u_i' u_j' u_k'}) \\
& - \frac{1}{\langle \rho \rangle} \left[ \frac{\partial}{\partial x_i} \overline{p' u_j'} + \frac{\partial}{\partial x_j} \overline{p' u_i'} \right] + \frac{\overline{p'}}{\langle \rho \rangle} \frac{\partial \overline{u_j'}}{\partial x_i} + \frac{\overline{p'}}{\langle \rho \rangle} \frac{\partial \overline{u_i'}}{\partial x_j} \\
& - \epsilon_{ikl} f_k \overline{u_j' u_l'} - \epsilon_{jkl} f_k \overline{u_i' u_l'} + \frac{g}{\langle \theta_v \rangle} \left[ \overline{u_j' \theta_v'} \delta_{i3} + \overline{u_i' \theta_v'} \delta_{j3} \right] \\
& + \nu \left[ \frac{\partial^2 \overline{u_i' u_j'}}{\partial x_k \partial x_k} - 2 \frac{\partial \overline{u_i' u_j'}}{\partial x_k \partial x_k} \right]. \tag{12}
\end{aligned}$$

Similarly, cross-multiplying Eqs. (9) and (10) by  $s'$  and  $u_i'$ , adding, and Reynolds averaging, gives

$$\begin{aligned}
\frac{\partial}{\partial t}(\overline{u_i' s'}) + \frac{\partial}{\partial x_k}(U_k \overline{u_i' s'}) = & - \overline{u_k' s'} \frac{\partial U_i}{\partial x_k} - \overline{u_i' u_k'} \frac{\partial S}{\partial x_k} \tag{13} \\
& - \frac{\partial}{\partial x_k}(\overline{u_i' u_k' s'}) - \frac{1}{\langle \rho \rangle} \frac{\partial (\overline{p' s'})}{\partial x_i} + \frac{\overline{p'}}{\langle \rho \rangle} \frac{\partial \overline{s'}}{\partial x_i} - \epsilon_{ikl} f_k \overline{s' u_l'} \\
& + \frac{\overline{s' \theta_v'}}{\langle \theta_v \rangle} \delta_{i3} g + \frac{\partial}{\partial x_k} \left[ \nu s' \frac{\partial \overline{u_i'}}{\partial x_k} + \gamma_s \overline{u_i' \frac{\partial s'}{\partial x_k}} \right] - (\nu + \gamma_s) \overline{\frac{\partial s'}{\partial x_k} \frac{\partial u_i'}}{\partial x_k}.
\end{aligned}$$

Thus, we now have equations which describe the dynamic behavior of the momentum and scalar fluxes,  $\overline{u_i' u_k'}$  and  $\overline{u_i' s'}$ , which appear in the averaged Eqs. (5) and (6). However, examination of Eqs. (12) and (13) show that a problem of closure still exists. Additional unknowns (e.g., terms involving triple velocity correlations, pressure-velocity correlation, etc.) appear in these expressions. Again a method of reducing the number of unknowns at this stage may be sought, or still more equations which describe the behavior of these new unknowns may be developed. Should the latter course be selected, the new set of equations would contain an increasing number of unknown terms. This is the fundamental nature of the turbulence closure problem and arises from the nonlinearity of turbulent flows. Once the turbulent field was decomposed into a mean and a perturbation, the full detail concerning the flow's

instantaneous behavior could only be reconstructed with knowledge of all ensemble-average statistics of all turbulent moments.. Fortunately, our goals are always considerably more modest.

### 2.1.2 Closure Relationships and the Full Set of Equations

The term 'second-moment closure' derives from the fact that assumptions are made involving the unknown terms in the equations for the second moments (e.g., Eqs. (12) and (13)) which reduce the number of unknowns to the number of equations. The unknown terms are 'modeled' (i.e., the closure is effected) by relating them to terms involving the mean variables and the second moments.

Donaldson (1973) outlines some basic principles that provide guidance in the choice of closure assumptions. Of necessity, the closure assumptions are empirical in nature and model improvement and refinement depend upon experimental progress. The theoretical basis for many turbulence closure techniques is firmly rooted in the pioneering work of such investigators as Kolmogorov and Rotta.

Mellor (1973) and Mellor and Yamada (1974) developed a second-moment closure model for investigations of the PBL. Their modeling techniques were closely followed in the modeling development discussed here. The nature of the closure relationships used to treat the unknown terms in Eqs. (12) and (13) are now briefly outlined. Rotta's (1951) tendency towards isotropy term dealing with the energy redistributing properties of the pressure-velocity gradient terms is written as

$$\overline{\frac{p'}{\rho} \left( \frac{\partial u_j'}{\partial x_i} + \frac{\partial u_i'}{\partial x_j} \right)} = - \frac{q}{3\ell_i} (\overline{u_i' u_j'} - \frac{\delta_{ij}}{3} q^2) + C q^2 \left( \frac{\partial U_i}{\partial x_j} + \frac{\partial U_j}{\partial x_i} \right). \quad (14)$$

Here  $q^2 = \overline{u_i'^2}$ , which is twice the turbulent kinetic energy,  $\ell$  is a length scale and  $C$  is an empirical constant. The length scales and proportionality constants which appear in this and following closure expressions are taken from Mellor and Yamada (1974, 1977).

The triple correlation velocity and scalar diffusion terms are modeled as

$$\overline{u_i' u_j' u_k'} = - q \lambda_1 \left( \frac{\partial \overline{u_i' u_j'}}{\partial x_k} + \frac{\partial \overline{u_i' u_k'}}{\partial x_j} + \frac{\partial \overline{u_j' u_k'}}{\partial x_i} \right), \quad (15)$$



$$\overline{u_i' u_k' s'} = -q\lambda_2 \left( \frac{\partial \overline{u_i' s'}}{\partial x_k} + \frac{\partial \overline{u_k' s'}}{\partial x_i} \right). \quad (16)$$

The pressure diffusional terms are assumed to be negligible, thus,

$$\overline{p' u_j'} = \overline{p' s'} = 0. \quad (17)$$

Closure of the molecular dissipation term is based on the concept of local isotropy developed by Kolmogorov:

$$2\nu \frac{\partial \overline{u_i'}}{\partial x_k} \frac{\partial \overline{u_j'}}{\partial x_k} = \frac{2}{3} \frac{q}{\Lambda_1} \delta_{ij}. \quad (18)$$

Completing the necessary closures, we have

$$\frac{\overline{p'}}{\langle \rho \rangle} \frac{\partial \overline{s'}}{\partial x_i} = -\frac{q}{3\ell_2} \overline{u_i' s'}, \quad (19)$$

$$(\nu + \gamma_s) \frac{\partial \overline{s'}}{\partial x_k} \frac{\partial \overline{u_i'}}{\partial x_k} = 0. \quad (20)$$

As noted by Mellor (1973), this last relationship, Eq.(20), follows from the general requirement that the closure relationship has the same tensor properties as the term it replaces. Since this is a molecular diffusion term which is expected to exhibit local isotropy, and since there is no isotropic first-order tensor, this diffusion term is set to zero. In the above closure expressions,  $\lambda_1$ ,  $\lambda_2$ ,  $\Lambda_1$ , and  $\ell_2$  are all length scales which are proportional to each other, as discussed by Mellor and Yamada (1974).

Note that if  $i=j$  in Eq. (12) and the tensor contraction is performed, an equation for twice the turbulent kinetic energy,  $q^2$  is achieved. Now summarizing the general set of equations with the closure terms included, which forms the basis of the model equations:

$$\begin{aligned} \frac{\partial U_i}{\partial t} = & -\frac{\partial}{\partial x_k} [U_k U_i + \overline{u_i' u_k'}] - \frac{1}{\langle \rho \rangle} \frac{\partial p}{\partial x_i} - \epsilon_{ikl} f_k U_l \\ & + \left[ \frac{\theta_v - \langle \theta_v \rangle}{\langle \theta_v \rangle} - 1 \right] \delta_{i3} g + \nu \frac{\partial^2 U_i}{\partial x_k \partial x_k}, \end{aligned} \quad (21)$$

$$\frac{\partial \theta_\ell}{\partial t} = - \frac{\partial}{\partial x_k} [U_k \theta_\ell + \overline{u_k' \theta_\ell'}] + \gamma_\theta \frac{\partial^2 \theta_\ell}{\partial x_k \partial x_k} + \dot{Q}_{\text{rad}}, \quad (22)$$

$$\frac{\partial Q_w}{\partial t} = - \frac{\partial}{\partial x_k} [U_k Q_w + \overline{u_k' q_w'}] + \gamma_q \frac{\partial^2 Q_w}{\partial x_k \partial x_k}, \quad (23)$$

$$\frac{\partial U_i}{\partial x_i} = \frac{\partial u_i'}{\partial x_i} = 0, \quad (24)$$

$$\begin{aligned} \frac{\partial q^2}{\partial t} + \frac{\partial}{\partial x_k} (U_k q^2) = & - 2 \overline{u_i' u_k'} \frac{\partial U_i}{\partial x_k} + \frac{\partial}{\partial x_k} \left[ q \lambda_1 \left( \frac{\partial q^2}{\partial x_k} + 2 \frac{\partial \overline{u_i' u_k'}}{\partial x_i} \right) \right] \\ & + \frac{2g}{\langle \theta_v \rangle} \overline{u_i' \theta_v'} \delta_{i3} - \frac{2q^3}{\Lambda_1}, \end{aligned} \quad (25)$$

$$\begin{aligned} \frac{\partial}{\partial t} (\overline{u_i' u_j'}) + \frac{\partial}{\partial x_k} (U_k \overline{u_i' u_j'}) = & - \overline{u_j' u_k'} \frac{\partial U_i}{\partial x_k} - \overline{u_i' u_k'} \frac{\partial U_j}{\partial x_k} \\ & + \frac{\partial}{\partial x_k} \left[ q \lambda_1 \left( \frac{\partial \overline{u_i' u_j'}}{\partial x_k} + \frac{\partial \overline{u_i' u_k'}}{\partial x_j} + \frac{\partial \overline{u_j' u_k'}}{\partial x_i} \right) \right] \\ & - \frac{q}{3\ell_1} \overline{u_i' u_j'} - \frac{\delta_{ij} q^2}{3} + c q^2 \left( \frac{\partial U_i}{\partial x_j} + \frac{\partial U_j}{\partial x_i} \right) \\ & + \frac{g}{\langle \theta_v \rangle} [\overline{u_j' \theta_v'} \delta_{i3} + \overline{u_i' \theta_v'} \delta_{j3}] - \frac{2}{3} \frac{q^3}{\Lambda_1} \delta_{ij}, \end{aligned} \quad (26)$$

$$\begin{aligned} \frac{\partial}{\partial t} (\overline{u_i' \theta_\ell'}) + \frac{\partial}{\partial x_k} (U_k \overline{u_i' \theta_\ell'}) = & - \overline{u_k' \theta_\ell'} \frac{\partial U_i}{\partial x_k} - \overline{u_i' u_k'} \frac{\partial \theta_\ell}{\partial x_k} \\ & + \frac{\partial}{\partial x_k} \left[ q \lambda_2 \left( \frac{\partial \overline{u_i' \theta_\ell'}}{\partial x_k} + \frac{\partial \overline{u_k' \theta_\ell'}}{\partial x_i} \right) \right] - \frac{q}{3\ell_2} \overline{u_i' \theta_\ell'} + \frac{\overline{\theta_\ell' \theta_v'}}{\langle \theta_v \rangle} \delta_{i3} g, \end{aligned} \quad (27)$$

$$\begin{aligned} \frac{\partial}{\partial t} (\overline{u_i' q_w'}) + \frac{\partial}{\partial x_k} (U_k \overline{u_i' q_w'}) = & - \overline{u_k' q_w'} \frac{\partial U_i}{\partial x_k} - \overline{u_i' u_k'} \frac{\partial Q_w}{\partial x_k} \\ & + \frac{\partial}{\partial x_k} \left[ q \lambda_2 \left( \frac{\partial \overline{u_i' q_w'}}{\partial x_k} + \frac{\partial \overline{u_k' q_w'}}{\partial x_i} \right) \right] - \frac{q}{3\ell_2} \overline{u_i' q_w'} + \frac{\overline{\theta_v' q_w'}}{\langle \theta_v \rangle} \delta_{i3} g. \end{aligned} \quad (28)$$

Here  $\theta_\ell$  is the liquid water potential temperature (Betts, 1973; Deardorff, 1976);  $Q_w$ , the total water mixing ratio; and  $Q_{rad}$ , the radiative heating/cooling rate. These choices of thermodynamic variables are discussed later. Presently, it is only necessary to note that  $\theta_\ell$  and  $Q_w$  are quasi-conservative even in the presence of condensation.

Equations (25)-(28) contain the additional unknowns  $\overline{u_i' \theta_\ell'}$ ,  $\overline{\theta_\ell' \theta_\ell'}$  and  $\overline{\theta_\ell' q_w'}$ . Since  $\theta_\ell$  is not a conservative variable in the presence of condensation, the previously illustrated technique cannot be used to arrive at equations for these unknowns (e.g., we cannot simply put  $s' = \theta_\ell'$  in Eq. (13)). Instead, use is made of a procedure given by Yamada (1978), in which equations for  $\overline{\theta_\ell'^2}$ ,  $\overline{q_w'^2}$ , and  $\overline{\theta_\ell' q_w'}$  are developed. Then equations which relate  $\overline{u_i' \theta_\ell'}$ ,  $\overline{\theta_\ell' \theta_\ell'}$ , and  $\overline{\theta_\ell' q_w'}$  to these other variables are derived.

Therefore, first write Eq. (10) with  $s' = \theta_\ell'$  and then write it with  $s' = q_w'$ . Cross-multiplying by  $\theta_\ell'$  and  $q_w'$ , adding, and inserting the closure relationships yields

$$\begin{aligned} \frac{\partial \overline{\theta_\ell' q_w'}}{\partial t} + \frac{\partial}{\partial x_k} (U_k \overline{\theta_\ell' q_w'}) &= - \overline{u_k' q_w'} \frac{\partial \theta_\ell}{\partial x_k} - \overline{u_k' \theta_\ell'} \frac{\partial Q_w}{\partial x_k} \\ &+ \frac{\partial}{\partial x_k} \left( q \lambda_2 \frac{\partial \overline{\theta_\ell' q_w'}}{\partial x_k} \right) - \frac{\partial q}{\partial x_k} \overline{\theta_\ell' q_w'}. \end{aligned} \quad (29)$$

Equations for  $\overline{\theta_\ell'^2}$  and  $\overline{q_w'^2}$  are derived by multiplying Eq. (10) by  $s'$ , then replacing  $s'$  first with  $\theta_\ell'$  and then with  $q_w'$ ,

$$\frac{\partial \overline{\theta_\ell'^2}}{\partial t} + \frac{\partial}{\partial x_k} (U_k \overline{\theta_\ell'^2}) = - 2 \overline{u_k' \theta_\ell'} \frac{\partial \theta_\ell}{\partial x_k} + \frac{\partial}{\partial x_k} \left( q \lambda_3 \frac{\partial \overline{\theta_\ell'^2}}{\partial x_k} \right) - \frac{2q}{\lambda_2} \overline{\theta_\ell'^2}, \quad (30)$$

$$\frac{\partial \overline{q_w'^2}}{\partial t} + \frac{\partial}{\partial x_k} (U_k \overline{q_w'^2}) = - 2 \overline{u_k' q_w'} \frac{\partial Q_w}{\partial x_k} + \frac{\partial}{\partial x_k} \left( q \lambda_3 \frac{\partial \overline{q_w'^2}}{\partial x_k} \right) - \frac{2q}{\lambda_2} \overline{q_w'^2}. \quad (31)$$



With the aforementioned relations for  $\overline{u_i \theta_V}$ ,  $\overline{\theta_A \theta_V}$ , and  $\overline{\theta_V q_W}$  given by Yamada (1978), Eqs. (21)-(31) represent a closed set.

Use of the boundary layer approximation considerably simplifies this set of equations, and even further simplifications are possible. Through a systematic process of simplification based upon the degree of isotropy of the terms involved, Mellor and Yamada (1974, 1977) describe a hierarchy of turbulence closure models. Omitting details already described in their work, it is only necessary to state here that use is made of their 'level 3' approximation in which certain tendency and triple-correlation diffusion terms are neglected from the equations for the second moments.

### 2.1.3 Thermodynamic Variables and Treatment of Clouds

At this point, a return to the thermodynamic variables,  $\theta_\ell$  and  $Q_w$ , selected for the present model is warranted. The model previously used by Burk (1977) contained water vapor, but did not permit condensation. The thermodynamic variables of that model were virtual potential temperature,  $\theta_v$ , and specific humidity,  $Q$ . The fact that  $\theta_\ell$  and  $Q_w$  are quasi-conservative in the presence of condensation was an important factor in their selection for the present model, since it permitted the direct carryover of many of the model equations and techniques used in the earlier model.

Liquid water potential temperature,  $\theta_\ell$ , is related to potential temperature,  $\theta$ , absolute temperature,  $T$ , and liquid water specific humidity,  $Q_\ell$  by

$$\theta_\ell = \theta - \frac{\theta}{T} \frac{L}{c_p} Q_\ell . \quad (32)$$

Here  $c_p$  is the specific heat of dry air at constant pressure, and  $L$  is the latent heat of vaporization. The total water-substance specific humidity is given by

$$Q_w = Q + Q_\ell, \quad Q \leq Q_s , \quad (33)$$

where  $Q_s$  is the saturation specific humidity.

Using these thermodynamic variables, Sommeria and Deardorff (1977) and Mellor (1977) discuss a treatment of condensation which permits only a fraction of a grid volume to contain saturated air. In this method, the presence or absence of condensed water within a grid volume is not determined solely by the mean variables,  $\theta_\ell$  and  $Q_w$ . The turbulent fluctuations about the mean are also considered. In particular,  $\theta_\ell$  and  $Q_w$  are assumed to have a joint-normal probability distribution about the mean, with the model calculated quantities,  $\overline{\theta_\ell'^2}$ ,  $\overline{Q_w'^2}$ , and  $\overline{\theta_\ell' Q_w'}$  determining the size and shape of the distribution. Sommeria and Deardorff (1977) present an approximate method whereby the cloud fraction and liquid water content may be computed. Their method is used in this model.

#### 2.1.4 Radiative Transfer

For computation of radiative heating/cooling,  $Q_{rad}$ , I have been fortunate to be able to use directly the scheme developed at Aeronautical Research Associates of Princeton and discussed by Oliver et al. (1978).

This radiative scheme uses the two-stream approximation in which the direct solar and terrestrial thermal radiation fields are treated as separable. Beginning with the radiative transfer equation for a monochromatic beam of intensity  $I_\nu$ ,

$$\mu \frac{dI_\nu}{d\tau_\nu} = I_\nu - J_\nu, \quad (34)$$

and integrating through optical depth, over solid angle, and over bandwidth gives the radiative flux at some level  $z_1$  (either upward or downward flux depending upon direction of integration through optical depth). The result is

$$F_i^+(z_1) = \bar{F}^+(z_0) \beta_i(\tau_s - \tau_1) + \bar{J}(\tau_1) - \bar{J}(\tau_s) \beta_i(\tau_s - \tau_1) - \int_{z_0}^{z_1} \beta_i(\tau - \tau_1) \frac{d\bar{J}}{dz} dz, \quad (35)$$



$$F_i^-(z_1) = \bar{F}^-(H)\beta_i(\tau_1-\tau_H) - \bar{J}(\tau_1) - \bar{J}(H)\beta_i(\tau_1-\tau_H) - \int_H^{z_1} \beta_i(\tau-\tau_1) \frac{\partial \bar{J}}{\partial z} dz, \quad (36)$$

where  $J$  is the source function;  $H$  is a height above which we will not consider contributions to the downward flux;  $\mu$ , the cosine of the zenith angle;  $\nu$ , frequency;  $\beta$ , the transmission function; subscript  $i$  represents the bandwidth,  $\Delta\nu_i$ , over which the frequency integration has been performed; and the overbars represent average values within this bandwidth. The net flux at level  $z_1$  is

$$F_i^n(z_1) = F_i^+(z_1) + F_i^-(z_1). \quad (37)$$

The radiative heating/cooling rate is given by

$$\dot{Q}_{\text{rad}} = - \frac{\theta}{\langle \rho \rangle c_p T} \frac{dF_i^n}{dz}. \quad (38)$$

For terrestrial radiation, Rayleigh scattering is negligible and the source function,  $J$ , may be set equal to the Planck black body function. In doing so, local thermodynamic equilibrium is implicitly assumed. This is a good assumption in the lower atmosphere. Scattering of solar radiation is neglected, and emission at visible wavelengths is negligible, so that the source term for direct solar radiation is set to zero. The transmission functions used also take cloud liquid water into account as well as molecular absorption. (For details concerning the boundary flux values  $(\bar{F}^+(z_0), \bar{F}^-(z_0))$  and the selection of visible and infrared transmission functions, see Oliver et al. (1978).)

## 2.2 MODEL STRUCTURE AND BOUNDARY CONDITIONS

The grid structure in this model has high near-surface resolution with a non-uniform grid spacing. Aloft, the grid spacing is coarser and uniform. Similarity function relationships are used to provide the linkage between the prognostically computed grid

variables and the surface values. That is, the prognostically computed values at the second grid point above the surface and the surface values are used in conjunction with the stability-dependent similarity profiles to calculate the variables at grid point 1. The values at grid point 1 in turn influence the prognostic values through finite difference vertical derivatives. Barker and Baxter (1975) describe such a technique of treating the lower boundary conditions. Their scheme is used here by first calculating a bulk Richardson number,

$$Ri_B = \frac{g}{\bar{\theta}_v} \frac{z_2(\theta_{v2} - \theta_{v0})}{v_2^2} \quad (39)$$

where  $\bar{\theta}_v$  is the layer average virtual potential temperature,  $v^2 = u^2 + v^2$ , and subscript 2 refers to values at the second grid point above the surface. This bulk Richardson number is then used in conjunction with Eqs. (19)-(21) of Barker and Baxter (1975) to find the Monin-Obukhov length. Next, the surface scaling values  $u_*$ ,  $\theta_{v*}$ , and  $q_*$  are calculated and the values of  $u$ ,  $v$ ,  $\theta_v$  and  $Q$  at the first grid point are found from the similarity functions (Businger et al., 1971; Paulson, 1970).

Lower boundary conditions on the turbulent variables are found by assuming a near-surface production-dissipation balance in their dynamic equations. For example, in the turbulent kinetic energy (TKE) Eq. (25), the shear and buoyant production of TKE are required to be equal to the viscous dissipation rate. Thus, tendency, advection and triple-correlation diffusion terms are neglected. In the boundary layer approximation, the TKE equation then becomes

$$-\overline{u'w'} \frac{\partial U}{\partial z} + \frac{g}{\langle \theta_v \rangle} \overline{w'\theta_v'} = q^3/\Lambda_1, \quad (40)$$

where, for simplicity of notation, the surface stress is assumed to be aligned in the x-direction. This equation may be rewritten as

$$u_*^2 \left[ \frac{u_*}{kz} \phi_m(z/L) \right] - \frac{g}{\langle \theta_v \rangle} u_* \theta_{v*} = q^3/\Lambda_1, \quad (41)$$

where  $\phi_m$  is the nondimensional wind shear. Thus, the boundary condition on twice the TKE at grid point 1 is

$$q_1^2 = u_*^2 \left[ \frac{\Lambda_1}{kz_1} \phi_m \left( \frac{z_1}{L} \right) \right]^{2/3} - \left( \frac{g\Lambda_1}{\langle \theta_v \rangle} u_* \theta_{v*} \right)^{2/3} \quad (42)$$

In the previous work (Burk, 1977), logarithmic (law of the wall) relationships were used rather than the general similarity functions. This requires that  $z/L \ll 1$ , thus necessitating that the first several grid points be very close to the surface. The use of similarity functions helps relax this restriction somewhat.

For the simulations of the marine boundary layer discussed, sea surface temperature was held constant. Generally the oceanic surface roughness,  $z_0$ , is computed from an empirical formula (Charnock, 1955; Wu, 1969)

$$\frac{u_*^2}{gz_0} = 64.0 \quad (43)$$

where  $u_*$  is the surface friction velocity. The specific humidity at the sea surface is taken at its saturation value based on the sea surface temperature.

At the upper boundary, the turbulent fluxes and mean wind shears are assumed as zero, while the lapses of  $Q_w$  and  $\theta_L$  are held constant.

Numerical integration proceeds as described by Yamada and Mellor (1975), and Burk (1977). The difference equations are implicit and solved by the Thomas algorithm (von Rosenberg, 1975).



### 3. REFRACTIVE INDEX STRUCTURE FUNCTION COEFFICIENTS

The increasing use of remote sensing devices for probing the atmosphere demands intensified scrutiny of the nature of refractive index fluctuations, because these fluctuations often provide the scattering that the devices sense. Since atmospheric refractive index is wavelength dependent, the functional dependence of the refractive index structure parameter,  $C_n^2$ , is also dependent upon wavelength. Wesely (1976) used the well established formulas for refractive index in conjunction with the Kolmogorov-type 2/3 power law, Eq. (1), to derive expressions for acoustic, optical and microwave  $C_n^2$ .

The refractive index structure parameter of acoustic waves is generally found to be dependent primarily upon temperature fluctuations. Thus, Wesely (1976) formulates the acoustic  $C_n^2$  as

$$C_n^2 = [C_T^2/4T^2]\alpha_a^2, \quad (44)$$

where  $C_T^2$  is the temperature structure parameter and  $\alpha_a^2$  is a correction factor given by

$$\alpha_a^2 = 1 + r_{eT} \left( \frac{2DC_e T}{C_{TP}} \right) + \left( \frac{DC_e T}{C_{TP}} \right)^2. \quad (45)$$

Here,  $C_e$  is the square root of the water vapor pressure structure parameter, and can be directly related to the specific humidity structure parameter,  $C_q^2$ . The other terms in Eq. (45) are the mean pressure,  $P$ ; a constant,  $D$ , equal to 0.307; and the structural correlation coefficient

$$r_{eT} = C_{eT}^2 / (C_e C_T),$$

where  $C_{eT}^2$  is the crossed structure function coefficient.

The optical structure coefficient is also generally dependent primarily upon  $C_T^2$ , and Wesely (1976) formulates it in a similar fashion as

$$C_n^2 = [C_T^2 A_1^2 P^2 / T^4] \alpha_v^2, \quad (46)$$

where

$$\alpha_v^2 = 1 + r_{et} \left[ \frac{2(1-A_2/A_1)C_e T}{C_{Tp}} \right] + \left[ \frac{(1-A_2/A_1)C_e T}{C_{Tp}} \right]^2 \quad (47)$$

Here  $A_1$  and  $A_2$  are constants which appear in the equation for optical refractive index and are given by  $A_1 = 78.7 \times 10^{-6} \text{ K mb}^{-1}$  and  $A_2 = 66.3 \times 10^{-6} \text{ K mb}^{-1}$ .

Hence, the contributions of moisture fluctuations to the acoustic and optical structure parameters appear only through the correction factors  $\alpha_a$  and  $\alpha_v$ . Wesely and Alcaraz (1973) show that in the surface and in a free convection layer,  $\alpha_a$  and  $\alpha_v$  may be related to the local Bowen ratio (see Figures 1 and 2 of Wesely (1976)).

The refractive index structure parameter for microwaves has generally been found to be primarily dependent upon fluctuations in water vapor pressure, and Wesely (1976) writes

$$C_n^2 = \left[ \frac{C_e^2 A_3^2 (1-A_4/A_3)^2}{T^2} \right] \gamma_r^2, \quad (48)$$

where,

$$\gamma_r^2 = 1 + r_{eT} \left[ \frac{2C_{Tp}}{C_e T (1-A_4/A_3)} \right] + \left[ \frac{C_{Tp}}{C_e T (1-A_4/A_3)} \right]^2. \quad (49)$$

Here  $A_3 = 77.6 \times 10^{-6} \text{ K mb}^{-1}$  and  $A_4 = B+C/T$ , where  $B = 72 \times 10^{-6} \text{ K mb}^{-1}$  and  $C = 0.375 \text{ K}^2 \text{ mb}^{-1}$ .

Thus, Wesely (1976) provides a very complete development of the functional dependences of acoustic, optical and microwave refractive index structure parameters. However, there still remains the task of actually evaluating these functions throughout the PBL in a variety of circumstances. We need to know under what conditions the correction factors  $\alpha_a^2$ ,  $\alpha_v^2$ , and  $\gamma_r^2$  are near unity, and the extent to which these correction factors may be directly determined by the local Bowen ratio.



In order to evaluate Eqs. (44)-(49) with the turbulence closure model, expressions for  $C_T^2$ ,  $C_e^2$ , and  $C_{et}^2$  must be developed. Corrsin (1951) proposed an expression for the one-dimensional temperature spectrum in the inertial subrange which is dependent upon the rate of molecular destruction of temperature variance,  $\chi$ , and the rate of molecular dissipation of TKE,  $\epsilon$ . It can be shown (e.g., Wyngaard et al., 1971) that this leads to

$$C_T^2 = 1.6 \chi \epsilon^{-1/3} . \quad (50)$$

Based upon the previously described closure technique of treating the molecular dissipation terms, Eq. (50) may be written as

$$C_T^2 = 1.6 \frac{\overline{T'T'}}{\ell^{2/3}} . \quad (51)$$

Similarly, expressions relating  $C_e^2$  and  $C_{eT}^2$  can be developed which involve the rates of molecular dissipation of moisture variance, temperature-moisture covariance, and TKE (Wyngaard et al., 1978). Thus, expressions similar to Eq. (51) are written for  $C_e^2$  and  $C_{Te}^2$ . Wesely's (1976) relationships for acoustic, optical and microwave refractive index structure parameters may now be directly evaluated throughout the PBL. Again, it should be recalled that these computed structure functions will be based upon ensemble-averaged statistics and therefore cannot be directly related to a short-time-averaged structure function.

#### 4. MODEL EXPERIMENTS AND RESULTS

The results of several model experiments are described in this section, with particular emphasis upon refractive index structure functions within the PBL. The first two cases involve simulations of the marine planetary boundary layer (MPBL); an overland simulation is presented in Case C.

##### 4.1 CASE A

A numerical experiment similar to that of Sommeria (1976) is discussed in this case. Sommeria used an updated version of the Deardorff (1972) three-dimensional, subgrid-scale turbulence model which includes condensation to describe turbulent processes within an undisturbed trade wind boundary layer. Here, use is made of the same initial profiles of potential temperature, specific humidity, and wind as displayed in Figures 2-4 of Sommeria (1976), and the same initial and boundary conditions. The period of integration for this case was 6 h, which is about that used by Sommeria.

However, our specific humidity and potential temperature fields do not evolve in the same manner as in Sommeria (1976). Sommeria shows the specific humidity decreasing with time between the surface and ~550 m, while our model has specific humidity increasing within this layer (Figure 1). Since the surface specific humidity is assumed to be at saturation ( $22 \text{ gm kg}^{-1}$ ), the near-surface drying present in the Sommeria model is difficult to understand. It is true that there is dry air advection associated with the latitudinal ocean surface temperature variation of  $2 \times 10^{-3} \text{ K km}^{-1}$  southward. This corresponds to a  $2 \times 10^{-6} \text{ km}^{-1}$  saturation specific humidity variation southward. The maximum value of the meridional wind component,  $V_{\text{max}}$ , at  $t=3.71 \text{ h}$  in Sommeria's Figure 4 is about  $-0.45 \text{ ms}^{-1}$ . Using this  $V_{\text{max}}$  in conjunction with the latitudinal specific humidity gradient gives a specific humidity decrease due to advection of only  $1.2 \times 10^{-5}$  in 3.71 hr. Thus, horizontal advection of dry air cannot account for Sommeria's specific humidity decrease. Subsidence is not particularly strong in this case,

being equal to  $0.6 \text{ cm s}^{-1}$  at 2 km and decreasing linearly to zero at the surface. And, dry air entrainment from aloft does not appear capable of offsetting the upward moisture flux from the surface.

Clouds develop and grow in the region between 550 and 1450 m where the initial lapse is conditionally unstable. Maximum values of liquid content obtained are about  $0.5 \text{ g kg}^{-1}$ . Sommeria reports in-cloud liquid water contents of  $0.1\text{--}0.3 \text{ g m}^{-3}$ . However, the horizontally averaged value of liquid water content given by Sommeria is several orders of magnitude smaller than this value since only scattered cumuli develop in that 3-D model. In the 1-D model used here, it was hoped that the method of parameterization of condensation could, to a limited degree, distinguish between a stratus layer and a scattered cumulus situation. The Sommeria and Deardorff (1977) technique used in this model calculates not only the liquid water content, but also the cloud fraction. For scattered cumuli, the cloud fraction should be low, while it should be near unity within a stratus layer. The situation described in this experiment by the Sommeria model is a trade wind boundary layer containing patchy cumuli. But the cloud fraction which develops in the 1-D turbulence closure model is near unity, and thus indicative of stratus formation. The source of this discrepancy is not entirely evident and will require further investigation.

The calculation of acoustic, optical, and microwave structure parameters throughout the MPBL for Case A is now discussed. Rewriting Eqs. (44), (46), and (48) as

$$\text{(acoustic)} \quad c_n^2 = \frac{1}{4T^2} \left[ c_T^2 + \left( \frac{2DT}{p} \right) c_{eT}^2 + \left( \frac{DT}{p} \right)^2 c_e^2 \right], \quad (52)$$

$$\text{(optical)} \quad c_n^2 = \frac{A_1^2 p^2}{T^4} \left\{ c_T^2 + \left[ \frac{2(1-A_2/A_1)T}{p} \right] c_{eT}^2 + \left[ \frac{(1-A_2/A_1)T}{p} \right]^2 c_e^2 \right\}, \quad (53)$$

$$\begin{aligned} \text{(microwave)} \quad c_n^2 = & \frac{A_3^2 (1-A_4/A_3)^2}{T^2} \left\{ c_e^2 + \left[ \frac{2p}{T(1-A_4/A_3)} \right] c_{eT}^2 \right. \\ & \left. + \left[ \frac{p}{T(1-A_4/A_2)} \right]^2 c_T^2 \right\} \end{aligned} \quad (54)$$



permits examination of the individual contributions of  $C_T^2$ ,  $C_{et}^2$ , and  $C_e^2$  to  $C_n^2$ .

Figure 2 shows the vertical distribution of terms which comprise the acoustic  $C_n^2$  after 3 h integration in this case. Remarkably, the major contributor to  $C_n^2$  near the surface at this time is the third term in Eq. (52) involving  $C_e^2$ . The term involving  $C_T^2$ , which normally is the primary contributor to acoustic  $C_n^2$ , is negligible near the surface. Qualitative understanding of this behavior can be found in Figure 1. After 3 h integration, the near-surface vertical temperature gradient is very small, while substantial moisture lapse is still present. In the presence of these mean gradients, near-surface turbulence leads to relatively large moisture fluctuations as compared to those of temperature, and accounts for the enhanced importance of the  $C_e^2$  term.

Aloft in Figure 2, the situation is complex. All three terms in Eq. (52) contribute substantially to the acoustic  $C_n^2$ . The second term involving the temperature-moisture correlation is negative. The sharp peak in the distribution near 1.6 km is associated with the presence of clouds and the radiatively enhanced inversion near cloud top.

The functional dependence of the terms in Eq. (53) for optical  $C_n^2$  is the same as that in Eq. (52), except  $1-A_2/A_1$  ( $=0.158$ ) replaces  $D$  ( $=0.307$ ). Thus, the vertical distribution of terms making up the optical  $C_n^2$  after 3 h integration is very similar to that for acoustic  $C_n^2$  in Figure 2, but the first term is weighted slightly more.

The vertical distribution of microwave  $C_n^2$  after 3 h of integration in this case is shown in Figure 3. Here the contributions of the  $C_{Te}^2$  and  $C_T^2$  terms in Eq. (54) are negligible and the microwave structure parameter is determined solely by  $C_e^2$ . The profiles of these structure coefficients remain much the same through the remainder of the integration out to 6 h.

#### 4.2 CASE B

This case is a numerical experiment based upon data from the Cooperative Experiment in West Coast Oceanography and Meteorology of 1976 (CEWCOM-1976) (Bulletin AMS, 1977). Noonkester (1978a, 1978b) discusses detailed MPBL measurements made on 3 October 1976 near San Diego, California as a part of CEWCOM-1976. He presents acoustic sounder and FM-CW radar data showing the temporal behavior of an inversion-capped mixed layer.

This numerical experiment is begun by initializing the model with conditions thought to be representative of those at 1200 local time (LT). There were no radiosonde data at this time, so the initial temperature and specific humidity profiles are selected to be consistent with the later radiosonde profiles at 1850 LT and with the depth of the mixed layer (about 300 m) at 1200 LT as indicated by the acoustic sounder and FM-CW radar (Noonkester, 1978a; Figures 4 and 5). The initial wind field selected is guided by the bistatic acoustic wind data presented in Noonkester (1978b). The sea surface temperature is held fixed at 294°K, giving an initial 3°K temperature difference between the surface and 10 m. The surface specific humidity is set at its saturation value, and the surface roughness length is determined from an iterative technique using Eq. (43). Noonkester (1978a) notes the presence of subsidence during this experiment from the observed descent of a subsidence inversion from 2 km to 830 m between 0500 and 1700 LT on 3 October. To simulate this subsidence, a large-scale vertical velocity having magnitude  $-1 \text{ cm s}^{-1}$  at 1 km was specified. The vertical velocity is taken to decrease linearly to zero at the surface. The method of treating the other boundary and initial conditions has been discussed in Para. 2.2.

It was not the purpose of this experiment to emphasize comparisons of the model's evolution of the mean wind, temperature and humidity profiles with those of the actual data, although these fields are briefly examined. Rather, the goal was to examine the behavior of the individual terms contributing to the acoustic,

optical, and microwave structure parameters in this rather typical MPBL situation. But first, a brief discussion of the mean fields is warranted.

Figure 4 displays the evolution of the potential temperature and specific humidity fields. The mixed layer depth increases from 300 m initially at 1200 LT to 450 m at 1800 LT (the minimum in the virtual heat flux,  $-\overline{w'\theta'_v}$ , was used in conjunction with the potential temperature and moisture profiles to locate the top of the boundary layer,  $z_i$ ). This behavior of mixed layer depth is in reasonable agreement with the remote sounder data (Noonkester, 1978a; Figure 5).

Figure 5 displays the vertical profiles of the three terms in Eq. (52) which make up the acoustic refractive index structure parameter after one hour of integration (1300 LT). Near the surface; the term involving  $C_T^2$  is contributing about 65% of the total acoustic  $C_n^2$ ; the  $C_{Te}^2$  term about 30%; and  $C_e^2$  the remaining 5%. Aloft, the situation again is complex, with all three terms contributing substantially to  $C_n^2$ . The term involving  $C_{Te}^2$  is negative aloft. This term is dependent upon the temperature-moisture correlation,  $\overline{T'e'}$ , which is negative aloft due to the entrainment of warm, dry air from above the inversion. Note also that the peak in the acoustic  $C_n^2$  occurs at a height of 400 m, although the peak in the term involving  $C_e^2$  is located at 300 m. This will be discussed shortly.

Wyngaard et al. (1971) show by means of similarity theory that within the surface boundary layer

$$C_T^2 = T_*^2 Z^{-2/3} f(z/L), \quad (55)$$

where,

$$f(z/L) = \begin{cases} 4.9[1-7(z/L)]^{-2/3}, & z/L \leq 0 \\ 4.9[1+2.75(z/L)], & z/L \geq 0 \end{cases}$$



For free convection type conditions ( $-z/L \gg 1$ ), Eq. (55) becomes

$$C_T^2 = \frac{4}{3} T_*^2 (-L)^{2/3} z^{-4/3}. \quad (56)$$

Frisch and Ochs (1975) suggest a modification of Eq. (55) for inversion-capped boundary layers which is to be valid above the surface boundary layer:

$$C_T^2 = T_*^2 z^{-2/3} f(z/L) G(z/z_i), \quad (57)$$

where,  $G(z/z_i) = 1.0 + 0.84(z/z_i) + 4.13(z/z_i)^2$ ,

and  $0 \leq z/z_i < 0.8$ .

Here  $z_i$  is the inversion height.

Due to the near-surface moisture and temperature gradients in this case, the boundary layer is quite unstable (at 1300 LT,  $L = -12$  m). In the first 50 m, the  $C_T^2$  term in Figure 5 has a  $z^{-1.15}$  dependence. Under neutral conditions, Eq. (55) predicts a  $z^{-2/3}$  behavior. Thus, the  $C_T^2$  dependence in Figure 5 is bracketed between the  $z^{-4/3}$  free convection limit and the  $z^{-2/3}$  neutral boundary layer distribution. In fact, the distribution is very close to that predicted by Eq. (57) when the numerical values are inserted. However, above 100 m the model's  $C_T^2$  distribution does not agree with Eq. (57).

Again, the terms making up the optical structure parameter, Eq. (53), show much the same behavior as in Figure 5 since the functional dependence is very similar. Henceforth, there will be no discussion of the optical structure parameter since its behavior closely resembles the acoustic profiles.

The terms making up the microwave  $C_n^2$  at 1300 LT are displayed in Figure 6. Again, the first term in Eq. (54) involving  $C_e^2$  is the major contributor to microwave  $C_n^2$ . The peak in microwave  $C_n^2$  in Figure 6 occurs at 325 m. This does not coincide with the peak in the acoustic  $C_n^2$ , which as noted previously occurs at 400 m (Figure 5). Thus, if the average response of remote sounders were to behave in accordance with the profiles in Figures 5 and 6, then

an acoustic sounder would locate the base of the inversion 75 m higher than would an FM-CW radar. Noonkester (1978a) points out that such disagreement between acoustic sounders and FM-CW radars concerning the boundary layer mixing depth is quite common. In fact, on the day of this case study (3 October 1976), Noonkester reported that the acoustic mixing depth appeared to be greater than the radar depth between 1230 and 1315 LT, and between 1440 and 1645 LT with a maximum difference of up to 150 m. In the model, the acoustic mixing depth only differs from the radar microwave mixing depth between 1245 and 1330 LT. This occurs when  $C_T^2$ ,  $C_e^2$ , and  $C_{Te}^2$  do not all peak at the same elevation which, in turn, appears to be associated with the nature of the mean gradients of potential temperature and specific humidity. In an actively growing boundary layer, the base of the thermal inversion and the kink in the humidity profile where it markedly deviates from the mixed layer value may not always precisely coincide. This is the case in the model between 1245 and 1330 LT, with the thermal inversion being some 50 m higher than the specific humidity kink. Mixing in the vicinity of these gradients then results in temperature variance having a maximum slightly higher than the peak in specific humidity variance.

The model results at 1800 LT (Figures 7 and 8) are quite similar to those at 1300 LT. The microwave refractive index structure function is dominated by the  $C_e^2$  term in Eq. (54). Near the surface, the first term in Eq. (52) is contributing about 60% of the total acoustic  $C_n^2$ ; the second term about 35%; and the third term the remaining 5%.

However, there are some noteworthy changes which have occurred between 1300 and 1800 LT. The boundary layer has grown several hundred meters to a depth of 450 m. At 1800 LT the peaks in microwave and acoustic  $C_n^2$  aloft coincide. These peaks occur at 400 m and are sharper and of larger magnitude than those present at 1300 LT. These peaks are located at the top of a thin cloud layer which has developed.

#### 4.3 CASE C

The final numerical experiment is an overland case in which the surface temperature undergoes a substantial diurnal oscillation. Motivation for this overland case comes in part from a need to gain insight into just which processes are unique to the MPBL.

The initial and boundary conditions for this case are those used in Burk (1977). Briefly, the surface temperature and surface specific humidity are specified to undergo a diurnal wave (Figure 9), while the initial vertical distributions of wind and virtual potential temperature are as shown in Figure 10. The geostrophic wind is taken as a constant with height and time, having the value  $U_g = 18 \text{ ms}^{-1}$  and  $V_g = 0$ . The surface roughness length,  $z_0$ , is set at 1 cm, and the Coriolis parameter has a value of  $10^{-4} \text{ s}^{-1}$ , which corresponds to about  $43^\circ\text{N}$ .

The model experiment begins at 2000 LT and integrates through one diurnal cycle. In Burk (1977), emphasis was placed on the behavior of the specific humidity field. No clouds develop in this overland case. As in cases A and B, our prime concern is with the nature of acoustic, optical and microwave structure parameters.

Figure 11 shows that at 0000 and 0500 LT the acoustic index of refraction structure parameter,  $C_n^2$ , is primarily dependent upon the term involving  $C_T^2$  in Eq. (52). Aloft, the term involving  $C_{Te}^2$  also is contributing to the total  $C_n^2$ . The near-surface nocturnal values of acoustic  $C_n^2$  are relatively small compared to those which appear during midafternoon of this experiment, but they are comparable to the acoustic  $C_n^2$  values in cases A and B. The difference in the two profiles in Figure 11 is associated with the strengthening and sharpening of the nocturnal inversion during this period. The inversion top is located between 500 and 600 m at 0500 LT.

The situation in regard to the terms contributing to microwave  $C_n^2$  tends to be more complex in this overland experiment than in the MPBL simulations of cases A and B. Figure 12 shows the distributions of the three terms in Eq. (54) at 0000 and 0500 LT. Near the surface, all three terms make important contributions to



the total microwave  $C_n^2$ . Microwave  $C_n^2$  aloft is determined primarily by  $C_e^2$ , although the  $C_{Te}^2$  term still significant, particularly at 0500 LT where it has caused the peak in  $C_n^2$  to be located at 500 m rather than 550 m.

At 1500 LT, acoustic and optical  $C_n^2$  are primarily determined by  $C_T^2$  for heights below about 1 km (Figure 13). The inversion is at 1550 m. Near the inversion, all three terms in Eqs. (52) and (53) are important.

Wesely (1976) shows that if the ratio

$$R = \frac{C_e \overline{w^T T^T}}{C_T \overline{w^T e^T}}, \quad (58)$$

has an absolute value near unity, then the correction factors,  $\alpha_a^2$  and  $\alpha_v^2$ , in Eqs. (45) and (47) can be calculated based upon the local Bowen ratio. Figure 14 shows that below 1.2 km,  $|R|$  is near unity. Note that the height at which  $|R|$  first deviates from unity closely coincides with the height at which the structural correlation coefficient  $r_{et}$ , changes sign. At 1500 LT, the zero crossing of  $r_{et}$  occurs at ~1325 m ( $= 0.85 z_i$ ). In the region between  $0.85 z_i$ , and  $z_i$ , the influence of entrainment of warm, dry air from above (having negative  $\overline{\theta^T e^T}$ ) is very evident. Also note in Figure 13 that the acoustic  $C_n^2$  is closely following a  $z^{-4/3}$  distribution. The surface temperature is a maximum at this time and the boundary layer is quite unstable.

At 1500 LT, the first and second terms in Eq. (54) for microwave  $C_n^2$  are both rather large near the surface and of the same magnitude but opposite signs. The microwave  $C_n^2$  aloft shows a peak near the capping inversion, and its value is almost totally determined by the term involving  $C_e^2$ .

Finally, let us look at the situation at 1800 LT. Here some interesting results occur in the acoustic and optical refractive index parameters. Whereas at 0000 and 0500 LT the near-surface acoustic and optical  $C_n^2$  values were determined almost exclusively by  $C_T^2$ , at 1800 LT this is not the case (Figure 15). Near the surface, the first and second terms in Eq. (52) are near equal,

while the third term is somewhat smaller. All three terms aloft contribute in a complex manner to the total acoustic  $C_n^2$ . Also,  $C_T^2$  does not follow a  $Z^{-2/3}$  distribution despite the fact that the PBL is near-neutral ( $L = -810$  m). Wyngaard (1973) discusses the need for caution in applying similarity theory near sunrise or sunset due to the nonstationarity of the boundary layer. This seems to be the reason for the absence of the  $Z^{-2/3}$  behavior at 1800 LT. The microwave  $C_n^2$  at this time is determined almost solely by  $C_e^2$ .

## 5. CONCLUDING REMARKS

The make-up of the acoustic, optical and microwave index of refraction structure parameters has been investigated in this report. Clearly, a turbulence closure model such as described here has a great many other possible applications. For example, Oliver et al. (1978) use such a model in studying the interaction of the turbulence and radiation fields as fog and stratus develop. Yamada (1978), using a three-dimensional closure model in which some of the equations have been simplified, performs simulations of cloud development over a cooling pond.

Three separate numerical experiments are discussed. Cases A and B deal with rather typical MPBL situations. The final experiment (case C) is an overland simulation. The contributions of the three terms appearing in Eqs. (52)-(54) to the total acoustic, optical, and microwave refractive index structure parameters are examined.

The results of the experiments show significant differences between the marine boundary layer cases and the overland case insofar as the relative importance of the various terms contributing to these structure parameters is concerned. For instance, except when the boundary layer is near transition (sunrise and sunset), the acoustic and optical  $C_n^2$  over land are determined almost solely by  $C_T^2$  below the inversion. In the MPBL cases, however, the second and third terms in Eqs. (52) and (53) make important contributions to acoustic and optical  $C_n^2$ . Also, in the MPBL simulations, the term involving  $C_e^2$  is the prime determinant of microwave  $C_n^2$ ; whereas, near the surface in the overland case, all three terms in Eq. (54) are significant.

To an extent, these results may be interpreted in terms of Wesely's (1976) method of relating the correction factors  $\alpha_a^2$ ,  $\alpha_v^2$ , and  $\gamma^2$  in Eqs. (45), (47), and (49) to the Bowen ratio,  $\beta$ . Figures 1-3 of Wesely (1976) graphically display these relationships. Above land typically  $|\beta| > 0.5$ , and Wesely's figures show that  $\alpha_a$  and  $\alpha_v$  should be near unity. Thus, overland acoustic and optical  $C_n^2$  should be determined primarily by  $C_T^2$  as found above.



However, when  $|\beta| > 0.5$ , Wesely (Figure 3) shows that  $\gamma_r$  can differ significantly from unity, meaning that overland  $C_{Te}^2$  and  $C_T^2$  may contribute significantly to microwave  $C_n^2$ . Again, this is what we found, at least near the surface.

Over the ocean surface  $|\beta|$  may be small. Thus  $\gamma_r$  should be near unity, while  $\alpha_a$  and  $\alpha_v$  may differ significantly from unity. This also is consistent with our findings.

There are situations, however, in which the Wesely relationships based upon local Bowen ratio cannot be utilized. The ratio  $|R|$  in Eq. (58) must be near unity for the Wesely relations to hold. Both in the overland case and the MPBL cases,  $|R|$  close to the surface was almost always found to be near unity. Similarly, the magnitude of the structural correlation coefficient,  $|r_{et}|$ , is always found to be close to unity near the surface in these experiments except for short periods near sunrise and sunset. However, aloft in a convective boundary layer,  $r_{et}$  changes sign. In the vicinity of the zero crossing of  $r_{et}$ , the moisture and heat fluxes are weak and the triple correlation diffusion terms which appear in the equations for the turbulent moments are important. At and above the zero crossing of  $r_{et}$ ,  $|R|$  is no longer typically close to unity (Figure 14).

Although the optical structure parameter has not been emphasized here, it should be stated that the model results are consistent with measured values of this quantity. Wesely and Alcaraz (1973) discuss the diurnal cycle of optical refractive index structure function coefficients in a variety of circumstances. In their Figure 10 they present results of measurements of optical  $C_n^2$  above grass at the electromagnetic propagation range of the U.S. Army Ballistic Research Laboratories, Aberdeen Proving Ground, Maryland. The measurements were made during the spring above a moist, grassy surface. These conditions are similar to those assumed for case C. In our Figure 16 we reproduce these measured values of optical  $C_n^2$  and also the  $C_n^2$  values from case C at 5 and 10 m above the surface. The degree of agreement in Figure 16 certainly may be somewhat fortuitous since case C was not specifically designed to simulate the conditions present at the observation

site. However, the general agreement is encouraging. Wesely and Alcaraz (1973) also point out that cloud cover caused the low  $\zeta_n^2$  values measured between 1600 and 1800 LT.

An effort is being initiated to examine these model results further and to compare them with a more extensive atmospheric data set. The influence of stratus and fog on the structure coefficients will also be investigated. It is recognized that such detailed boundary layer investigations may necessitate revisions in the turbulence closure model. This continual need to revise one's model is an integral part of the empiricism of numerical modeling which, although humbling, represents progress.

#### ACKNOWLEDGMENTS

I wish to express my thanks to Dr. T. Yamada for helpful discussions concerning modeling techniques. Also, I am indebted to Dr. W. S. Lewellen and his colleagues of the Aeronautical Research Associates of Princeton for supplying the radiative transfer subroutine which was used in this model. Drs. T. Rosmond and A. Weinstein of NEPRF provided helpful support and encouragement to this project. Finally, I thank Mr. S. Bishop for his thorough editing of this manuscript, AGI J. Carlson for his careful drafting of the figures, and Ms. W. Carlisle for her patient and accurate typing.



## REFERENCES

- Barker, E. H., and T. L. Baxter, 1975: A note on the computation of atmospheric surface layer fluxes for use in numerical modeling. J. Appl. Meteor., 14, No. 4, 620-622.
- Betts, A. K., 1973: Non-precipitating cumulus convection and its parameterization. Quart. J. Roy. Meteor. Soc., 99, 178-196.
- Burk, S. D., 1977: The moist boundary layer with a higher order turbulence closure model. J. Atmos. Sci., 34, No. 4, 629-638.
- Businger, J. A., J. C. Wyngaard, Y. Izumi and E. F. Bradley, 1971: Flux profile relationships in the atmospheric surface layer. J. Atmos. Sci., 28, No. 2, 181-189.
- Charnock, H., 1955: Wind stress on a water surface. Quart. J. Roy. Meteor. Soc., 81, 639-640.
- Corrsin, S., 1951: On the spectrum of isotropic temperature fluctuations in an isotropic turbulence. J. Appl. Phys., 22, No. 4, 469-473.
- Deardorff, J. W., 1972: Numerical investigation of neutral and unstable planetary boundary layers. J. Atmos. Sci., 29, No. 1, 91-115.
- \_\_\_\_\_, 1976: Usefulness of liquid-water potential temperature in a shallow-cloud model. J. Appl. Meteor., 15, No. 1, 98-102.
- Donaldson, C. duP., 1973: Construction of a dynamic model of the production of atmospheric turbulence and the dispersal of atmospheric pollutants. In Workshop on Micrometeorology, ed. D. Haugen; Boston: Amer. Meteor. Soc., 313-392.
- Friehe, C. A., J. C. LaRue, F. H. Champagne, C. H. Gibson, and G. F. Dreyer, 1975: Effects of temperature and humidity fluctuations on the optical refractive index in the marine boundary layer. J. Opt. Soc. Am., 65, No. 12, 1502-1511.
- Frisch, A. S., and G. R. Ochs, 1975: A note on the behavior of the temperature structure parameter in a convective layer capped by a marine inversion. J. Appl. Meteor., 14, No. 3, 415-419.
- Fritz, R. B., and R. S. Lawrence, 1977: WSMR atmospheric structure constant. NOAA tech. memo. ERL WPL-27.
- Gossard, E. E., 1960: Power spectrum of temperature, humidity and refractive index from aircraft and tethered balloon measurements. IEEE Trans. Antennas Propagation, AP-3, 186-201.

- \_\_\_\_\_, 1978: The distribution of radio refractive index structure parameter on boundary layers undergoing spatial or temporal transition. Radio Sci., 13, No. 2, 255-259.
- Kolmogorov, A. N., 1941: The local structure of turbulence in incompressible viscous fluid for very large Reynolds' numbers. C. R. Akad. Nauk SSSR, 30, 301-305. Transl., Friedlander, S. K., and Topper, L., Eds., 1961: Turbulence Classic Papers on Statistical Theory, Interscience.
- Mellor, G. L., 1973: Analytic prediction of the properties of stratified planetary surface layers. J. Atmos. Sci., 30, No. 6, 1061-1069.
- \_\_\_\_\_, 1977: The Gaussian cloud model relations. J. Atmos. Sci., 34, No. 2, 356-358. Corrigendum, J. Atmos. Sci., 34, No. 9, 1483-1484.
- \_\_\_\_\_, 1977: A turbulence model applied to geophysical fluid problems. Proc. Symp. on Turbulence Shear Flows, Penn. State Univ., PA, 249-281.
- \_\_\_\_\_, and T. Yamada, 1974: A hierarchy of turbulence closure models for planetary boundary layers. J. Atmos. Sci., 31, No. 7, 1791-1806. Corrigendum, J. Atmos. Sci., 34, No. 9, 1482.
- Noonkester, V. R., 1978a: Multi-sensor measurements of ocean based convective activity. 18th Conf. on Radar Meteor., Atlanta, GA, 55-64.
- \_\_\_\_\_, 1978b: Acoustic echosounder, acoustic bistatic wind and FM-CW radar measurements during west coast foehn winds. Fourth Symp. Meteor. Observ. and Instru., Denver, CO, 447-454.
- O'Brien, J. J., 1970: A note on the vertical structure of the eddy exchange coefficient in the planetary boundary layer. J. Atmos. Sci., 27, 1213-1215.
- Oliver, D. A., W. S. Lewellen, and G. G. Williamson, 1978: The interaction between turbulent and radiative transport in the development of fog and low-level stratus. J. Atmos. Sci., 35, No. 2, 301-316.
- Paulson, C. A., 1970: The mathematical representation of wind speed and temperature profiles in the unstable atmospheric surface layer. J. Appl. Meteor, 9, No. 6, 857-861.
- Sommeria, G., 1976: Three-dimensional simulation of turbulent processes in an undisturbed trade wind boundary layer. J. Atmos. Sci., 33, No. 2, 216-241.

- \_\_\_\_\_, and J. W. Deardorff, 1977: Subgrid-scale condensation in models of nonprecipitating clouds. J. Atmos. Sci., 34, No. 2, 344-355.
- Tatarskii, V. I., 1961: Wave propagation in a turbulent medium. New York: McGraw-Hill Book Co. Inc., 285 pp.
- \_\_\_\_\_, 1971: The Effects of the Turbulent Atmosphere on Wave Propagation (Nauka, Moscow, 1967). Transl. from U.S. Dept. Comm. Nat. Tech. Inform. Serv., TT-68-50464, Springfield, VA.
- Taylor, G. I., 1935: Statistical theory of turbulence, pts. I-IV. Proc. Roy. Soc. London, 151A, 421-478.
- von Rosenberg, D. U., 1975: Methods for the numerical solution of partial differential equations. New York: American Elsevier Publishing Co., Inc., 128 pp.
- Wesely, M. L., 1976: The combined effect of temperature and humidity fluctuations on refractive index. J. Appl. Meteor., 15, No. 1, 43-49.
- \_\_\_\_\_, and E. C. Alcaraz, 1973: Diurnal cycles of the refractive index structure function coefficient. J.G.R., 78, No. 27, 6224-6232.
- \_\_\_\_\_, and Z. I. Derzka, 1975: Atmospheric turbulence parameters from visual resolution. J. Appl. Opt., 14, No. 5, 847-853.
- Wu, J., 1969: Froude number scaling of wind-stress coefficients. J. Atmos. Sci., 26, No. 3, 408-413.
- Wyngaard, J. C., 1973: On surface-layer turbulence. In Workshop on Micrometeorology, ed. D. Haugen; Boston: Amer. Meteor. Soc., 101-149.
- \_\_\_\_\_, and Y. Izumi, 1971: Behavior of the refractive-index-structure parameter near the ground. J. Opt. Soc. Am., 61, No. 12, 1646-1650.
- \_\_\_\_\_, W. T. Pennell, D. H. Lenschow, and M. A. LeMone, 1978: The temperature-humidity covariance budget in the convective boundary layer. J. Atmos. Sci., 35, No. 1, 47-58.
- Yamada, T., 1978: A three-dimensional, second-order closure numerical model of mesoscale circulations in the lower atmosphere. Argonne National Lab., ANL/RER-78-1.
- \_\_\_\_\_, and G. Mellor, 1975: A simulation of the Wangara atmospheric boundary layer data. J. Atmos. Sci., 32, No. 12, 2309-2329.



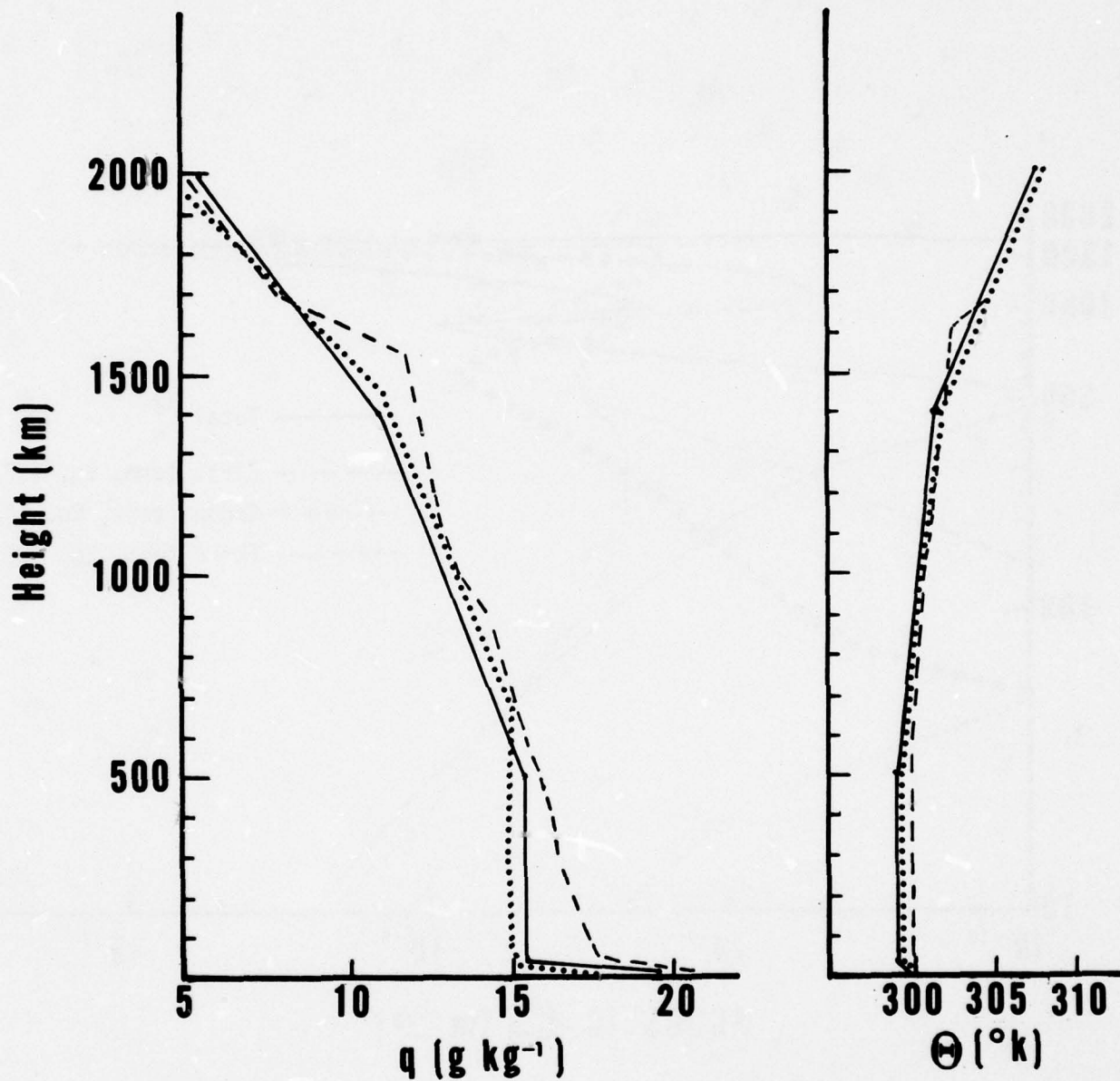


Figure 1. Profiles of specific humidity and potential temperature from case A. Solid line represents initial profiles; dotted line from Sommeria (1976) at  $t=3.71$  h; and, dashed line our model results at  $t=3$  h.

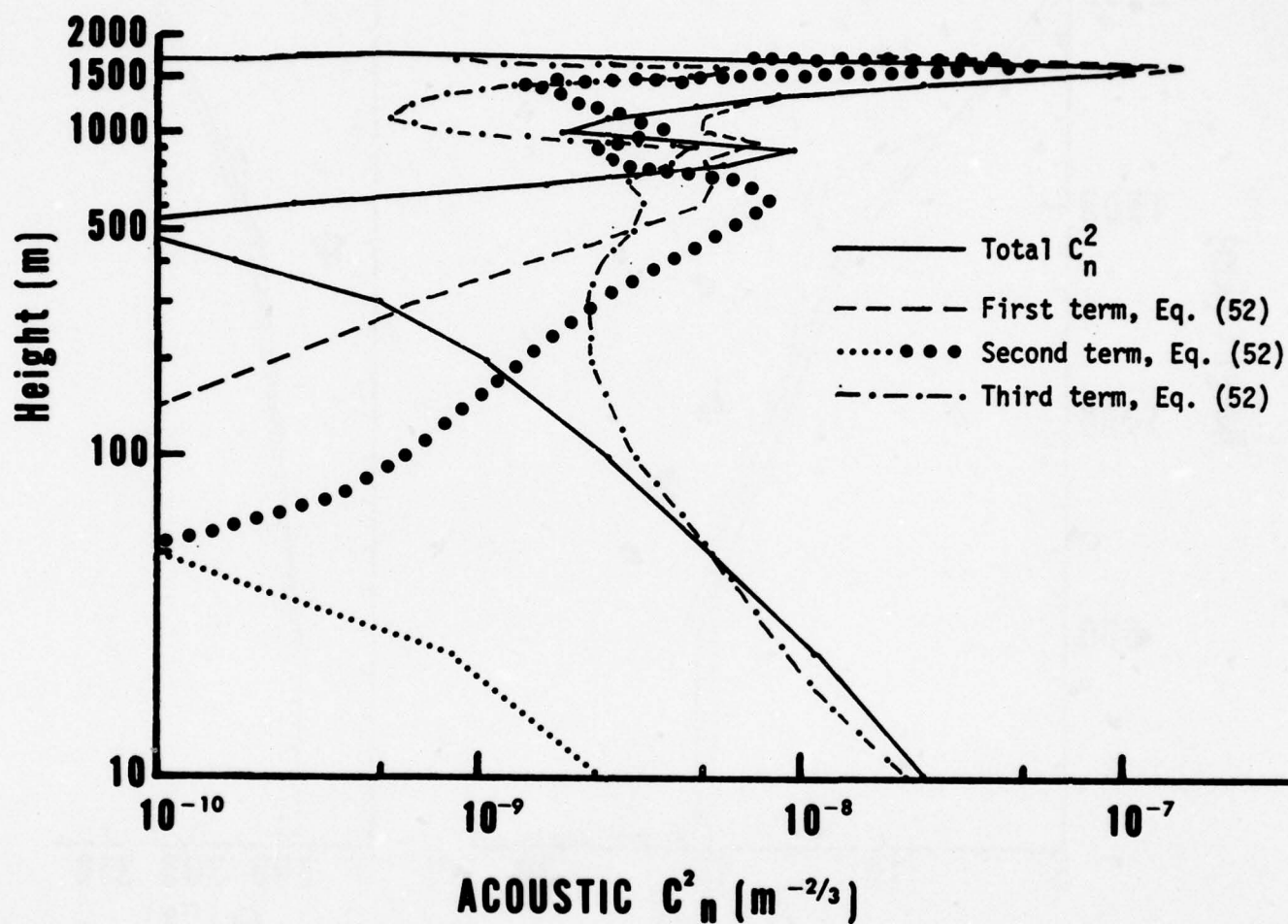


Figure 2. Vertical distribution of terms comprising acoustic  $C_n^2$  after 3 h integration in case A. Heavy dots represent negative values of second term in Eq. (52). Note that the sign of this second term is the same as that of  $C_{eT}$ .

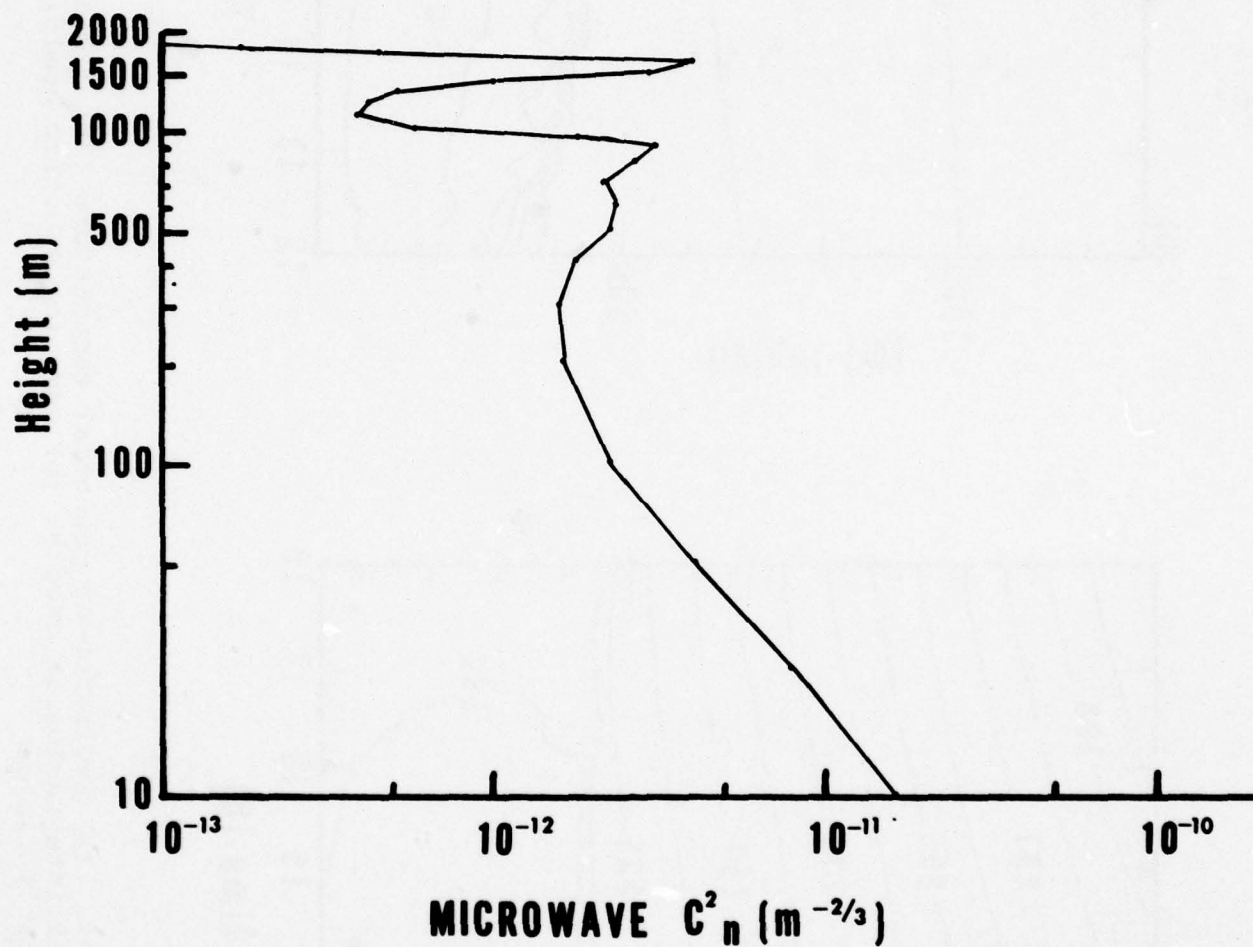


Figure 3. Vertical distribution of microwave  $C_n^2$  after 3 h integration in case A. Here total  $C_n^2$  is determined solely by first term in Eq. (54).



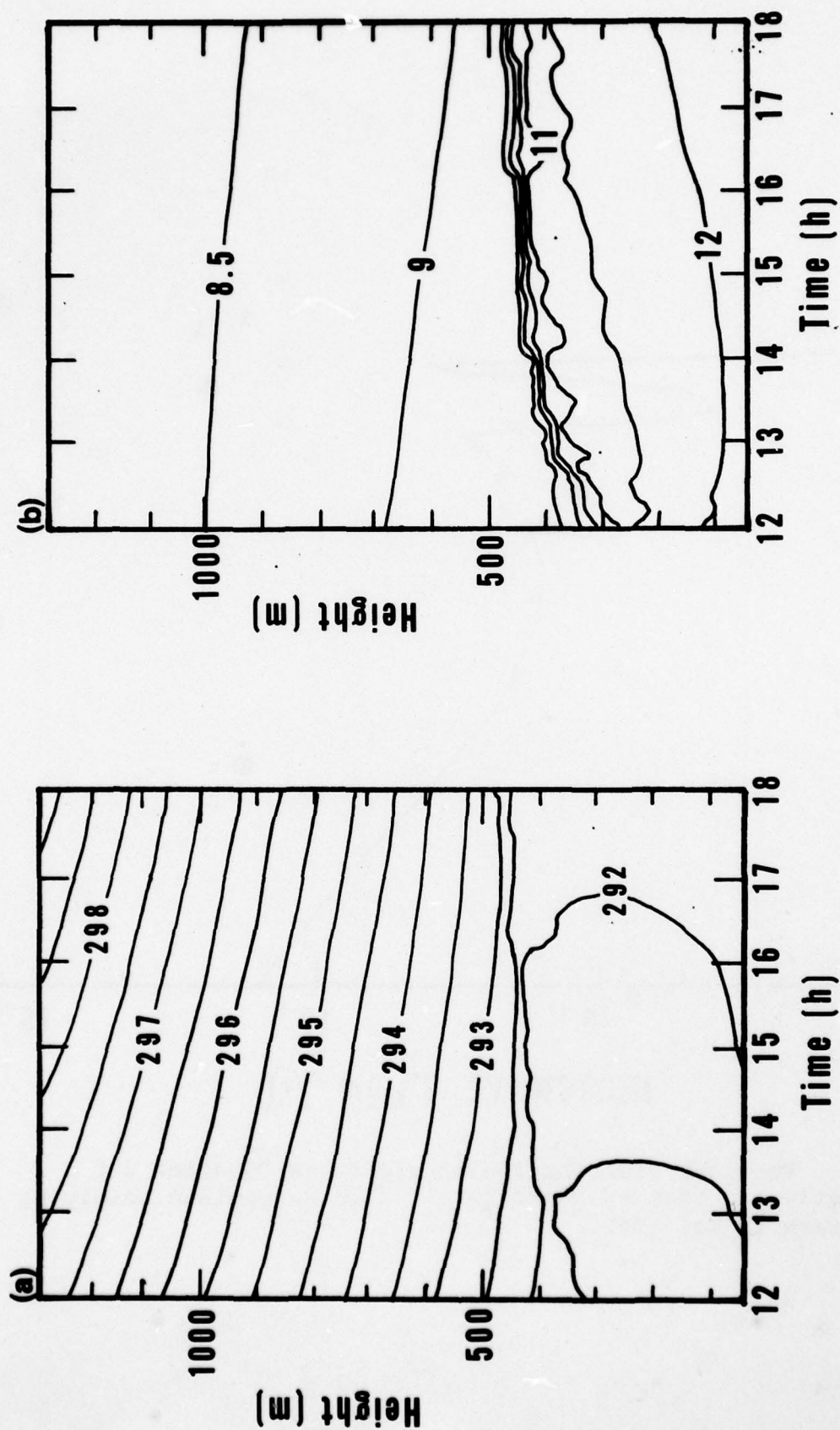


Figure 4. (a) Evolution of potential temperature ( $^{\circ}\text{K}$ ) field during 6 h of integration in case B; (b) same for specific humidity ( $\text{gm kg}^{-1}$ ) field.

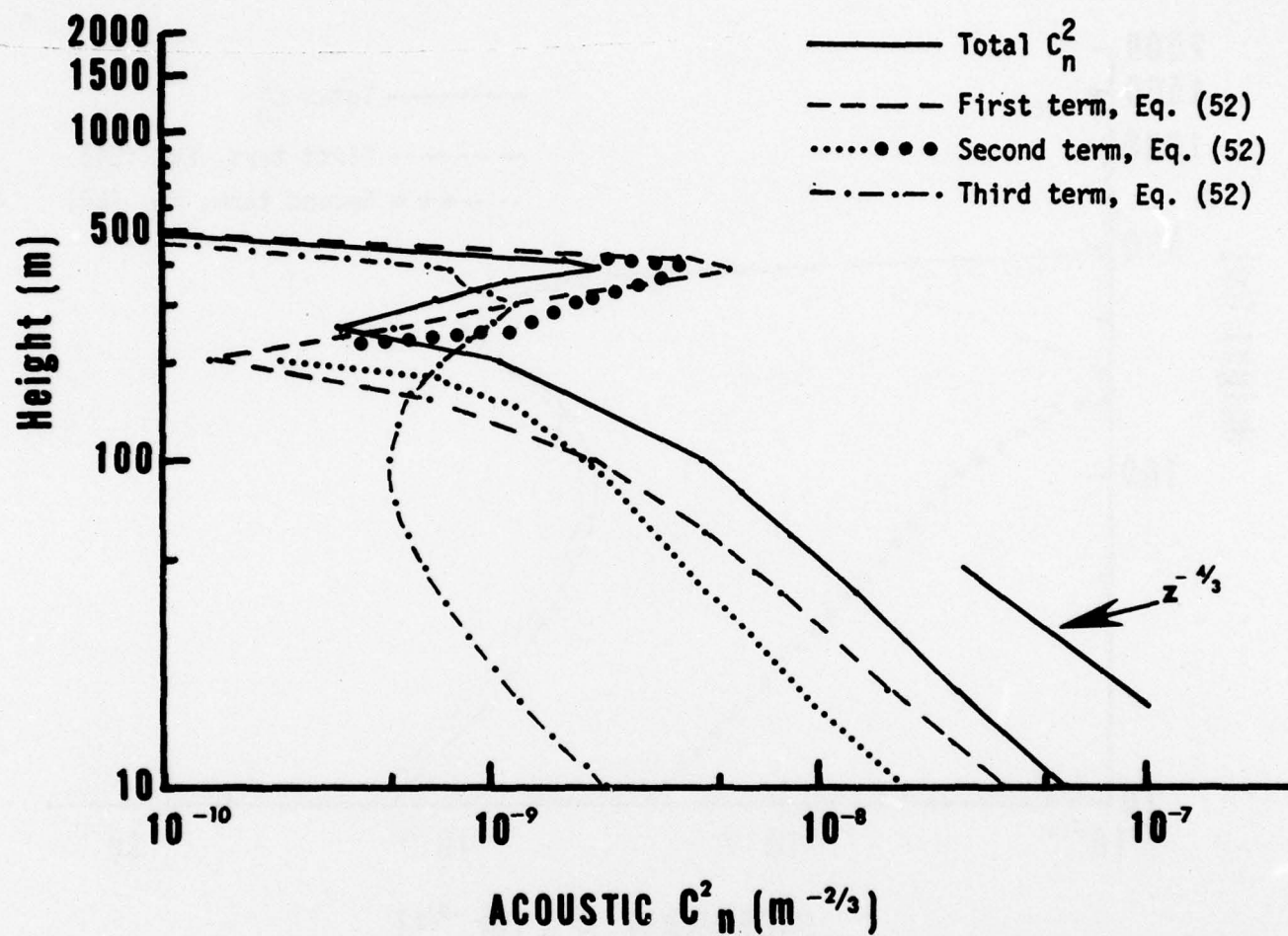


Figure 5. Vertical distribution of terms comprising acoustic  $C_n^2$  at 1300 LT in case B. Heavy dots represent negative values of second term in Eq. (52).

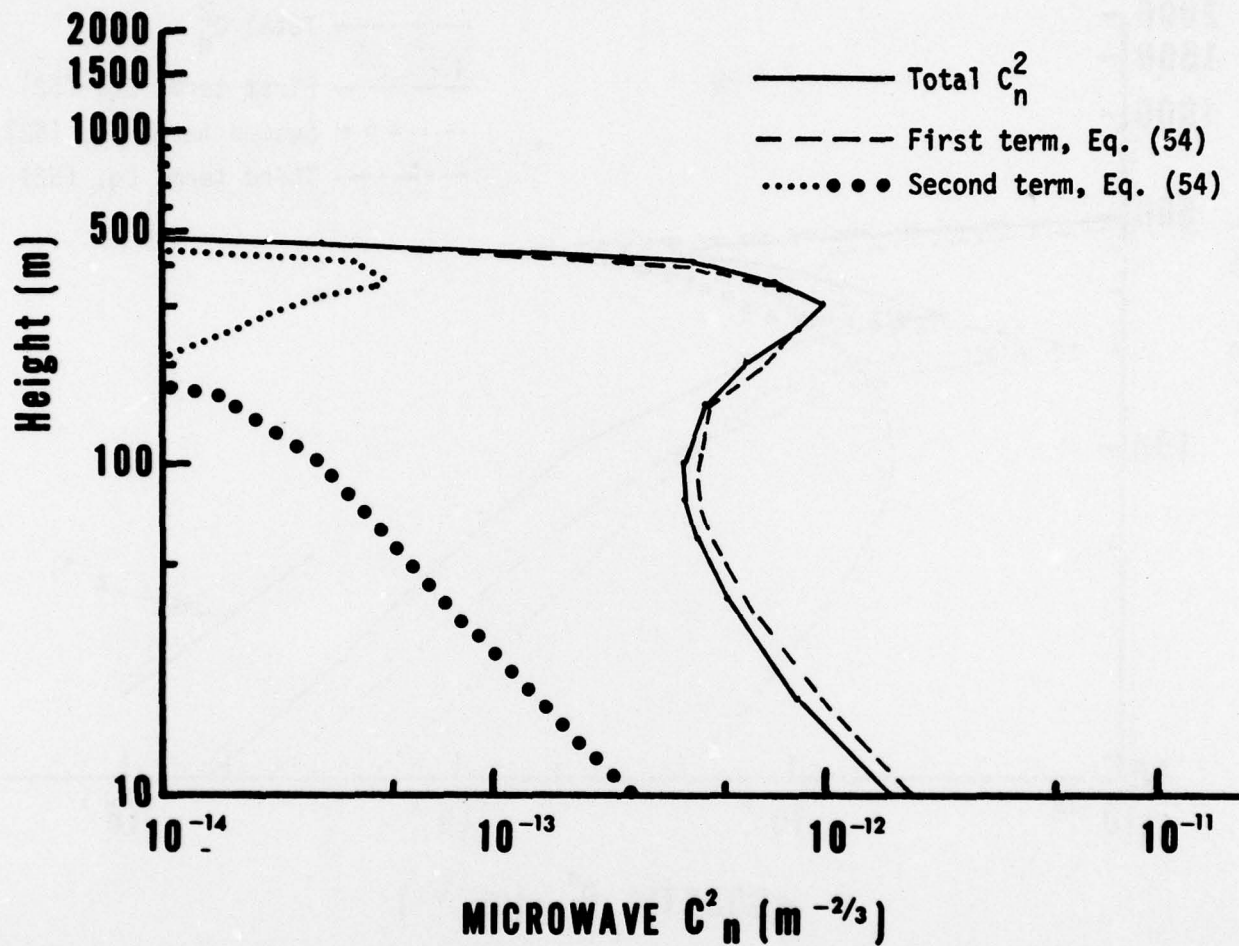


Figure 6. Vertical distribution of terms comprising microwave  $C_n^2$  at 1300 LT in case B. Heavy dots represent negative values of second term in Eq. (54). Note that the sign of the second term in Eq. (54) is different from that of  $C_{eT}$ .



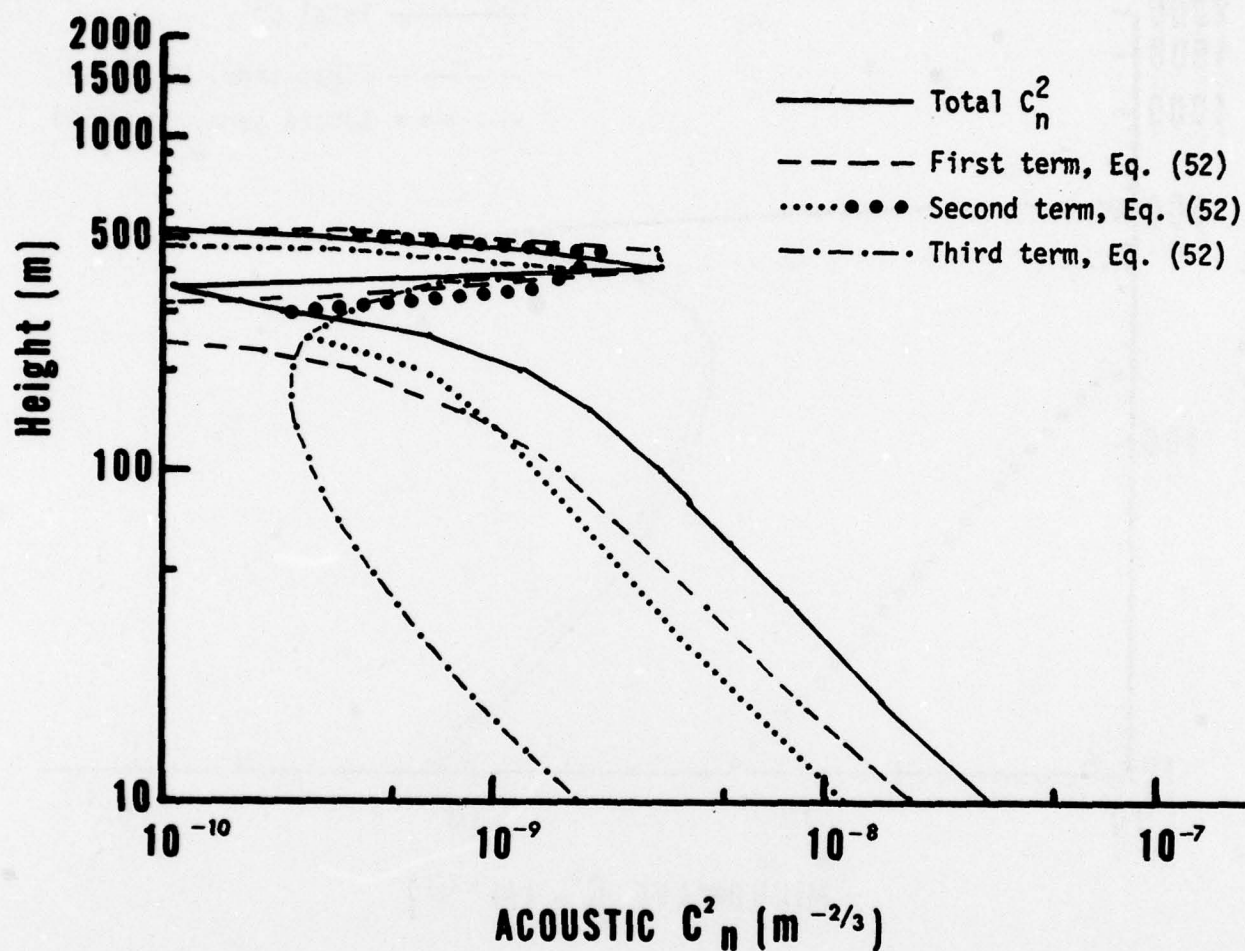


Figure 7. Vertical distribution of terms comprising acoustic  $C_n^2$  at 1800 LT in case B. Heavy dots represent negative values of second term in Eq. (52).

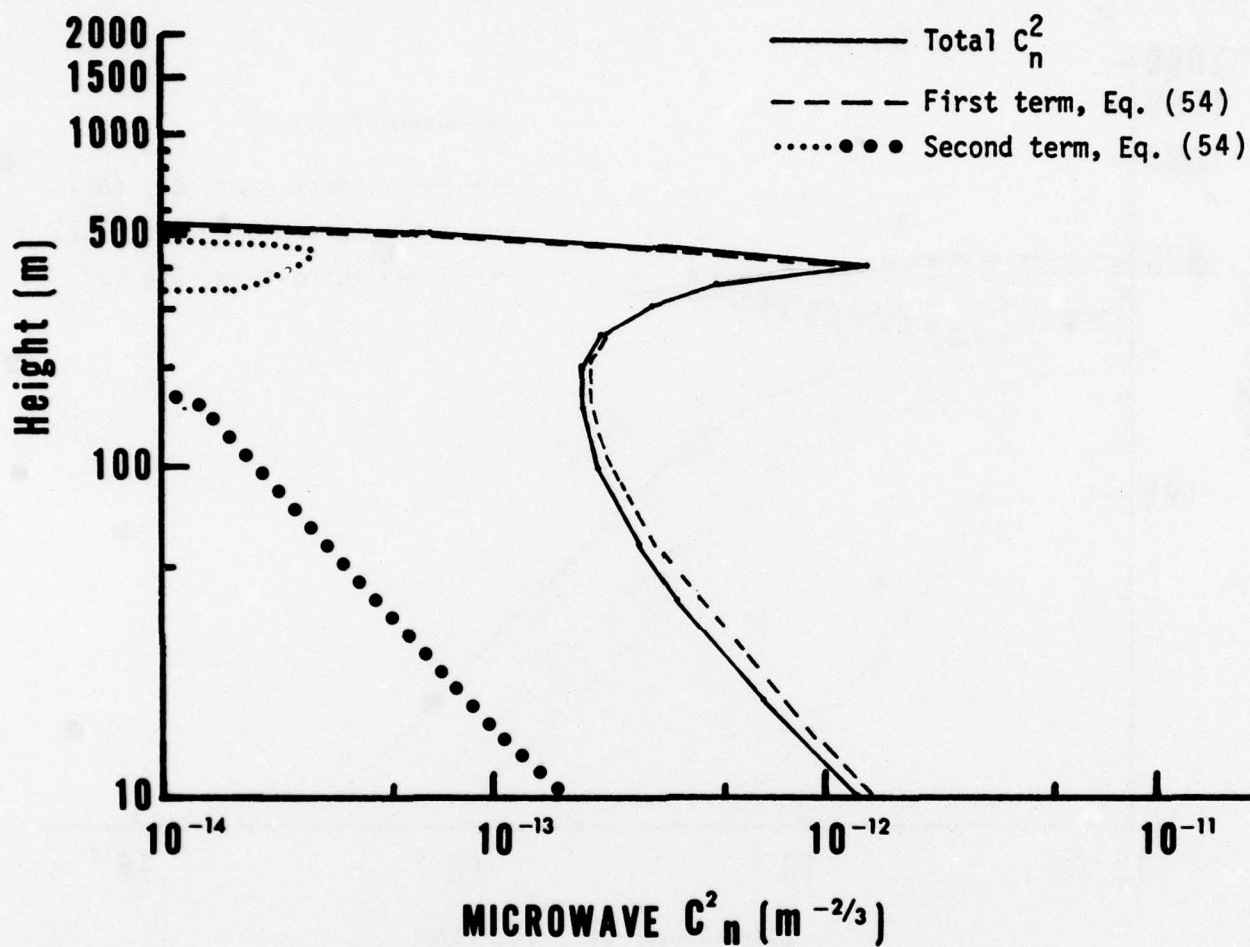


Figure 8. Vertical distribution of terms comprising microwave  $C_n^2$  at 1800 LT in case B. Heavy dots represent negative values of second term in Eq. (54).

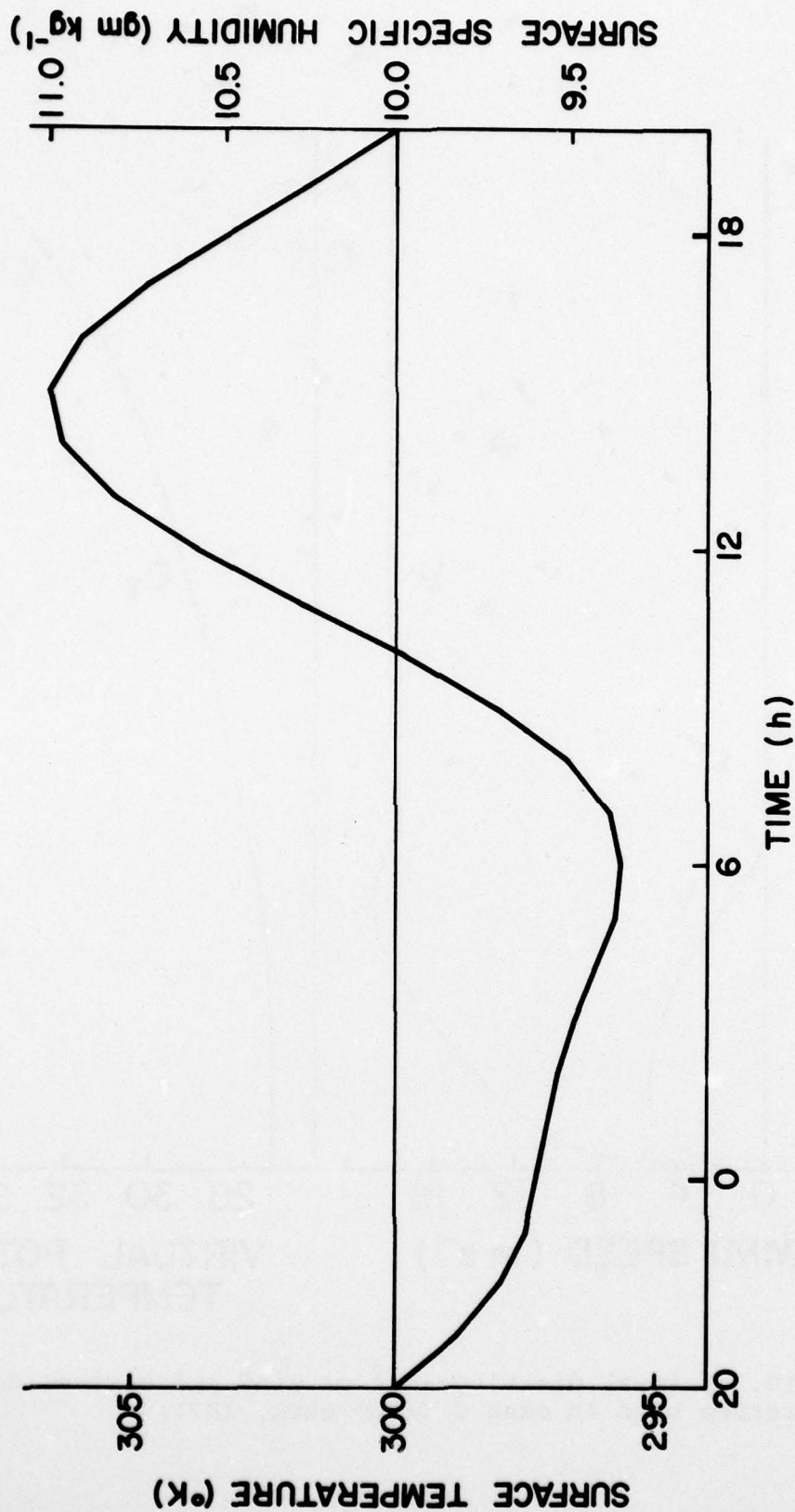


Figure 9. Specified diurnal variation of surface temperature and surface specific humidity in case C (from Burk, 1977).



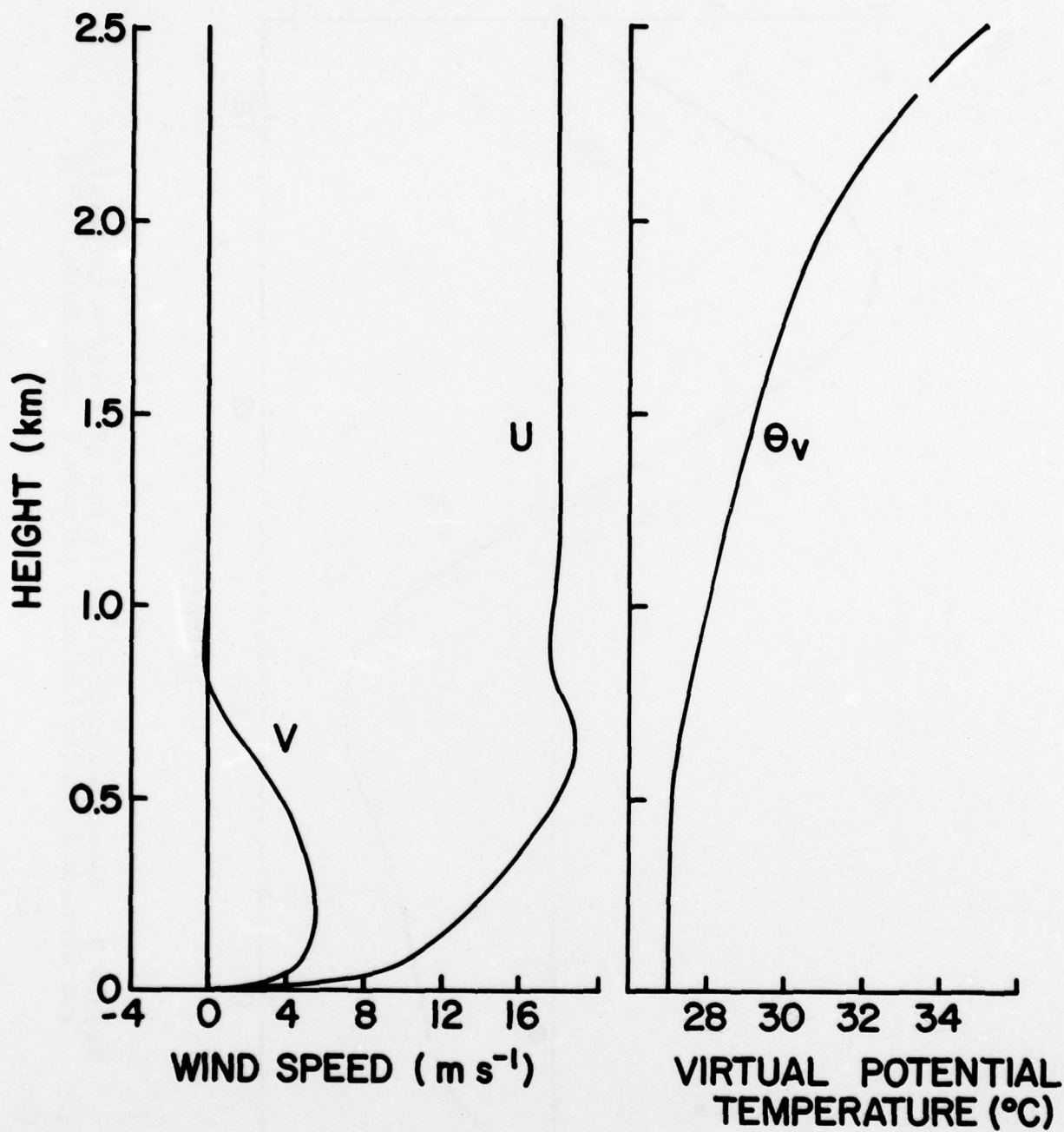


Figure 10. Initial distributions of wind and virtual potential temperature used in case C (from Burk, 1977).

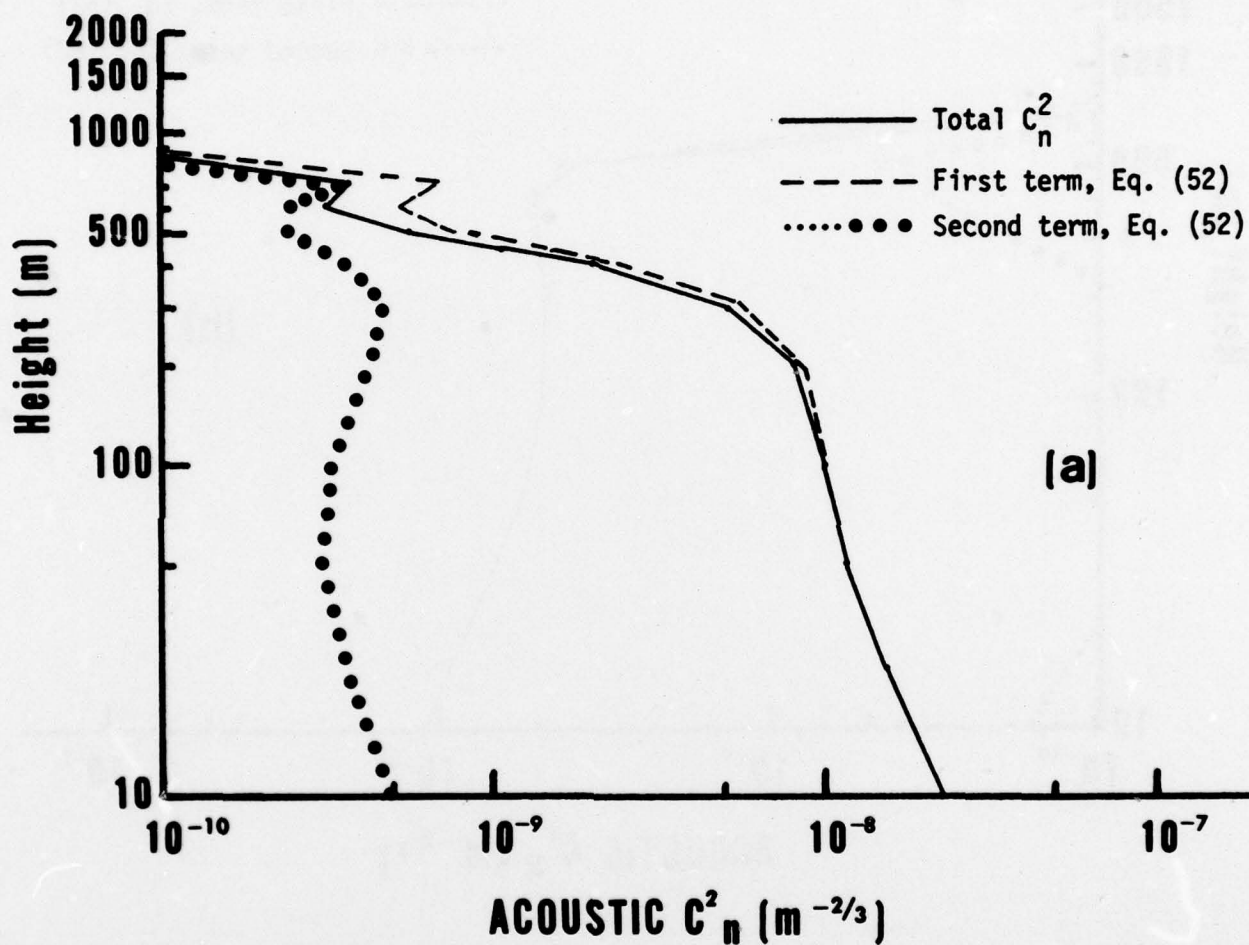


Figure 11. (a) Vertical distribution of terms comprising acoustic  $C_n^2$  at 0000 LT in case C; (b) at 0500 LT. Heavy dots represent negative values of second term in Eq. (52).

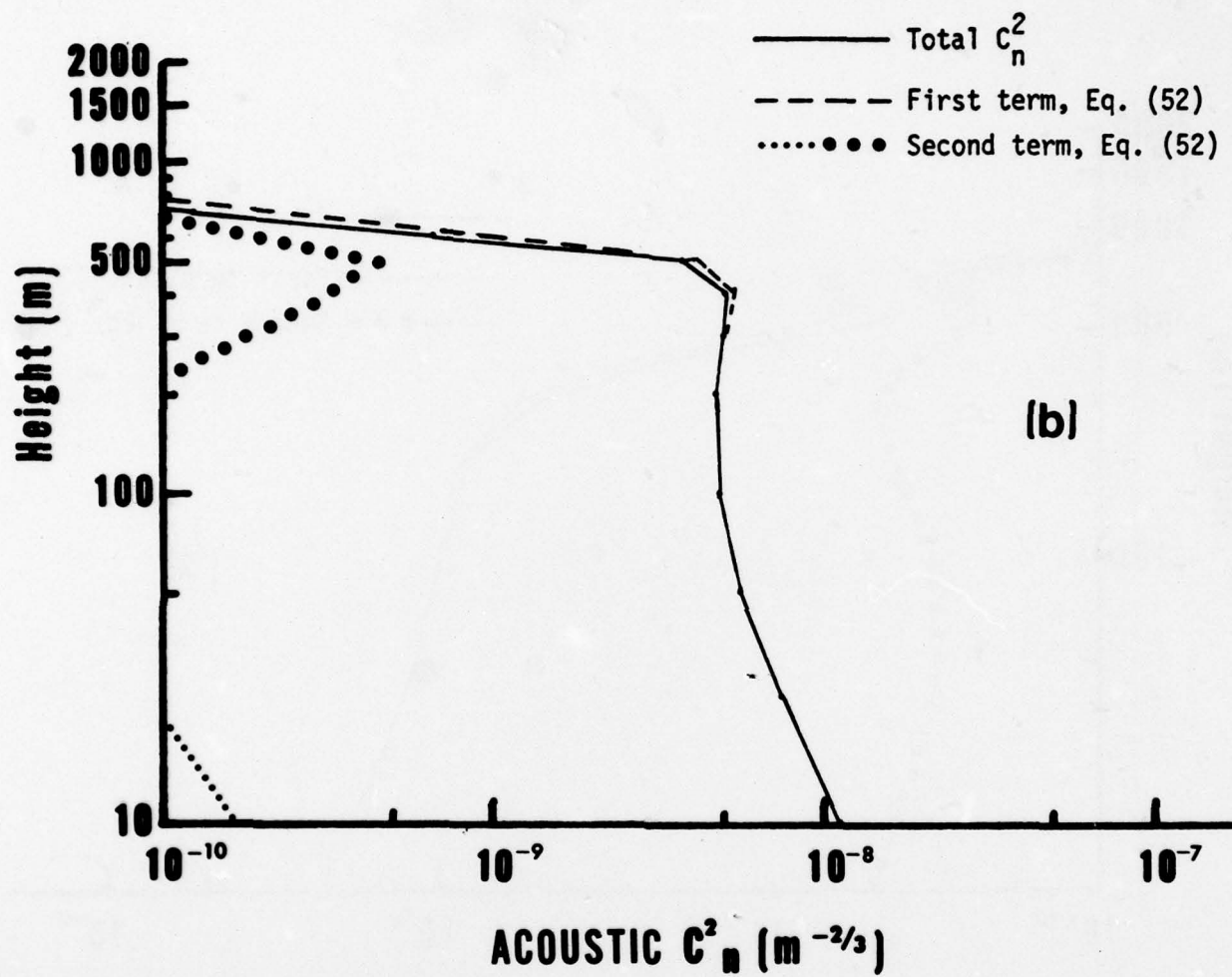


Figure 11, continued.



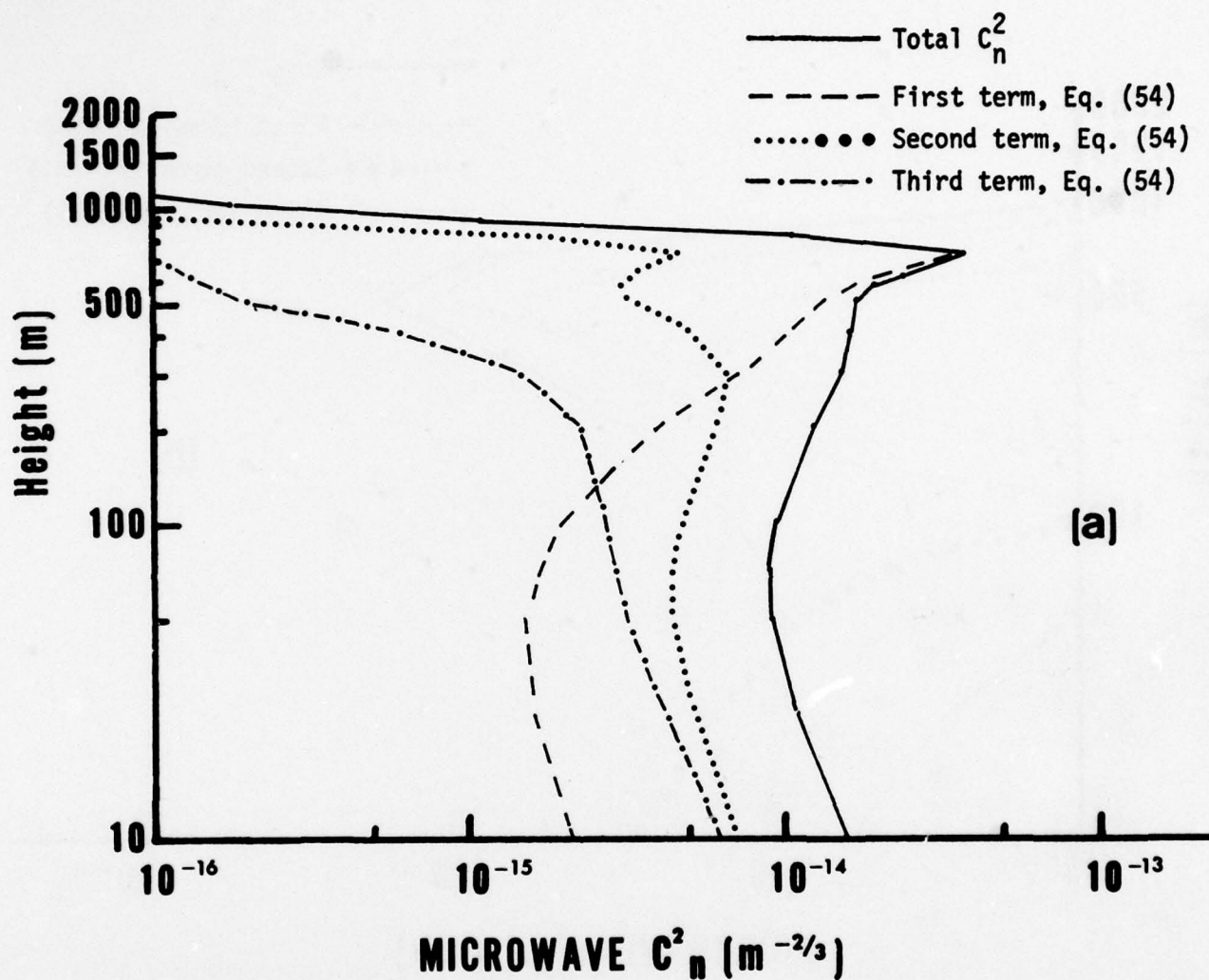


Figure 12. (a) Vertical distribution of terms comprising microwave  $C_n^2$  at 0000 LT in case C; (b) at 0500 LT. Heavy dots represent negative values of second term in Eq. (54).

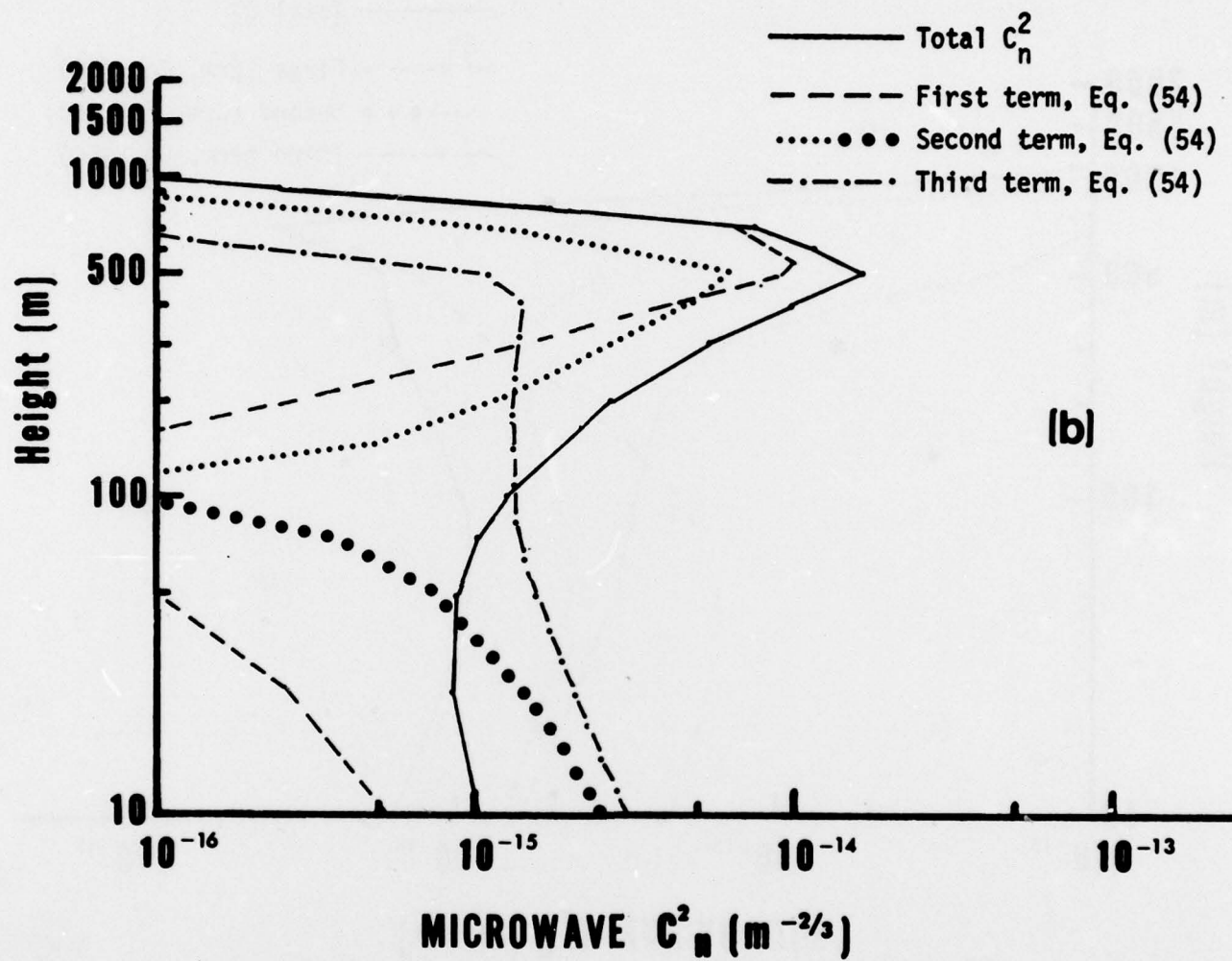


Figure 12, continued.

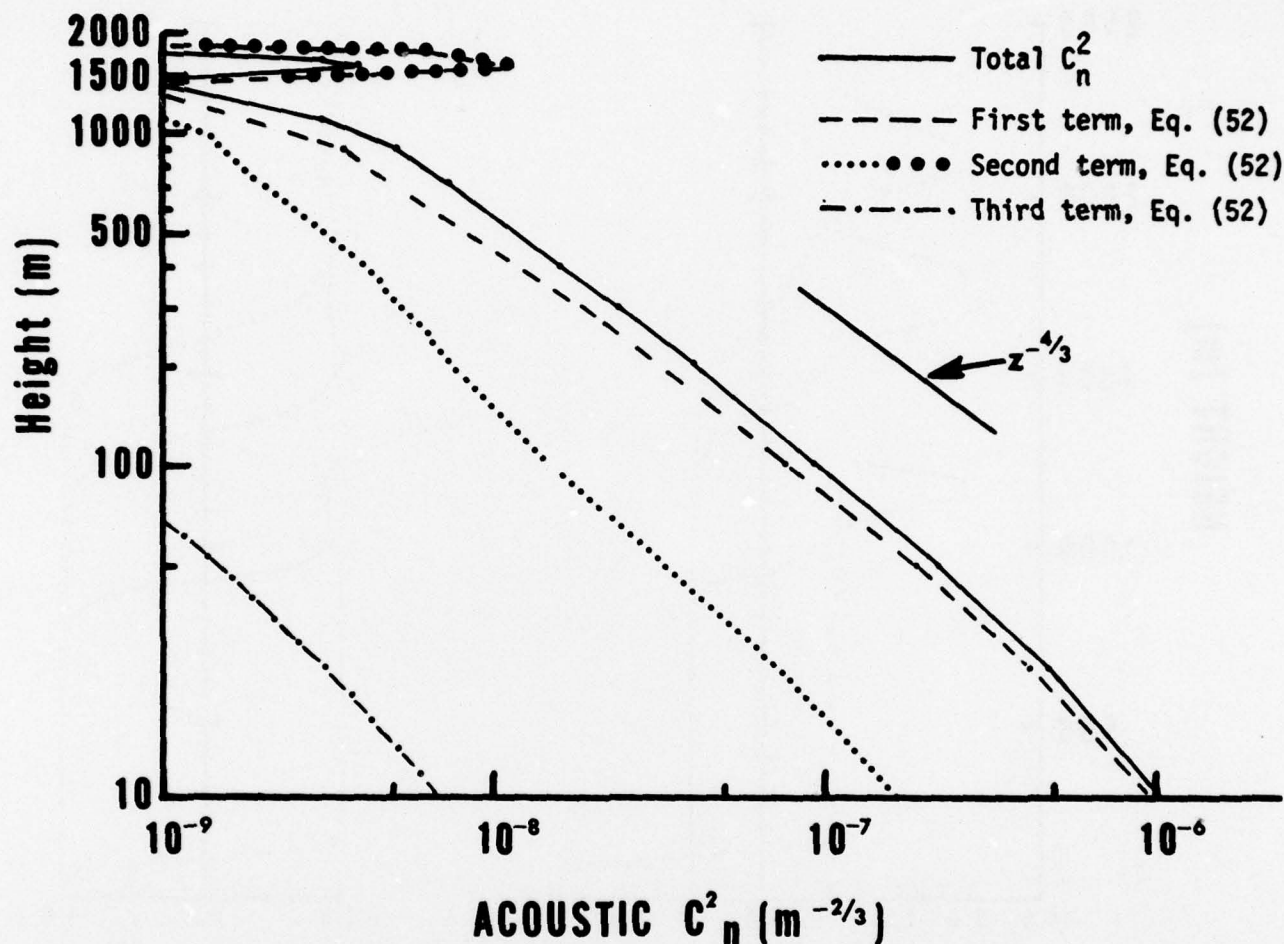


Figure 13. Vertical distribution of terms comprising acoustic  $C_n^2$  at 1500 LT in case C. Heavy dots represent negative values of second term in Eq. (52).



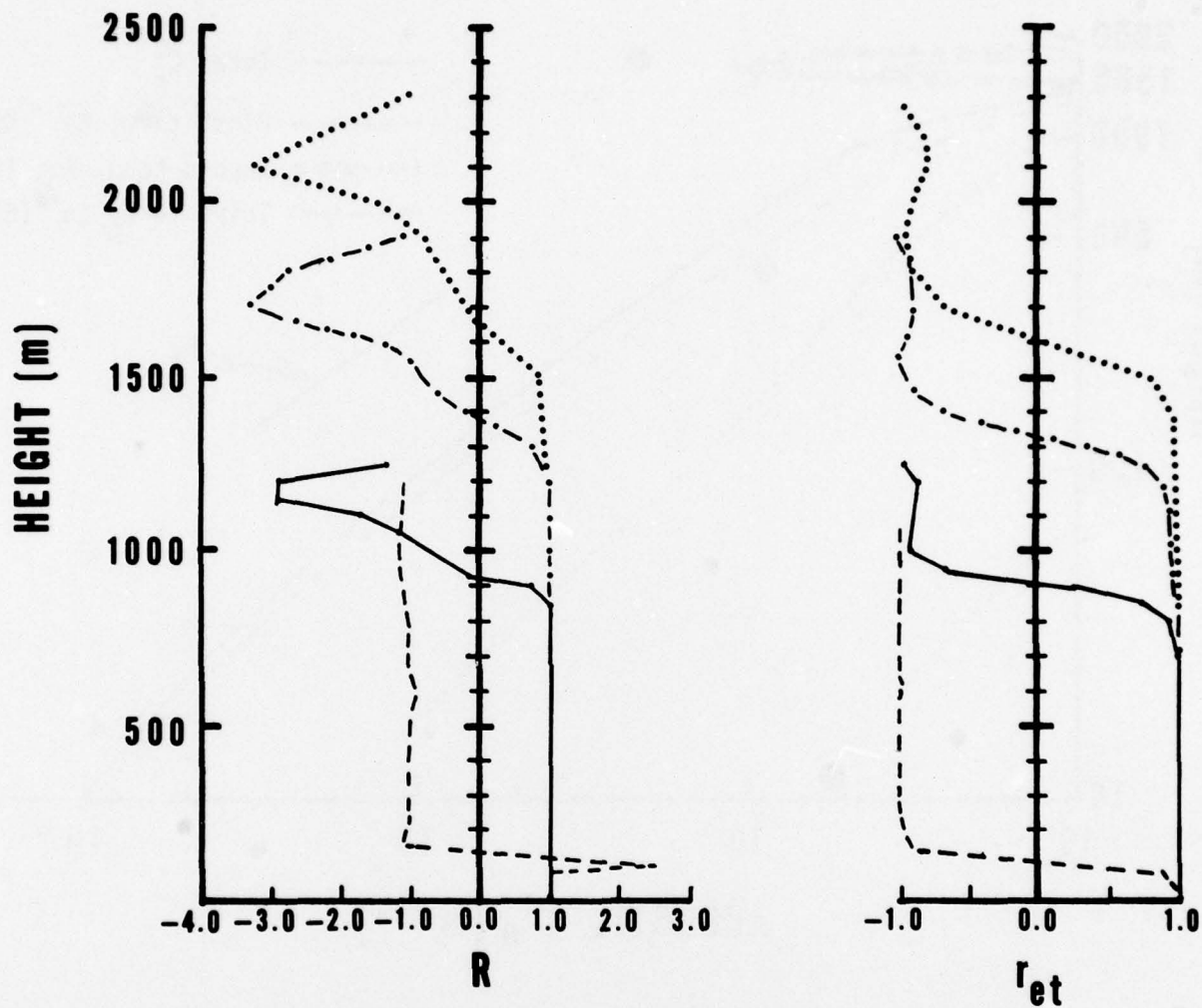


Figure 14. Profiles of the ratio,  $R$ , in Eq. (58), and  $r_{et}$  the structural correlation coefficient (see Eq. (45)) at various times in case C. Dashed, 0500 LT; solid, 1300 LT; dot-dash, 1500 LT; dotted, 1800 LT.

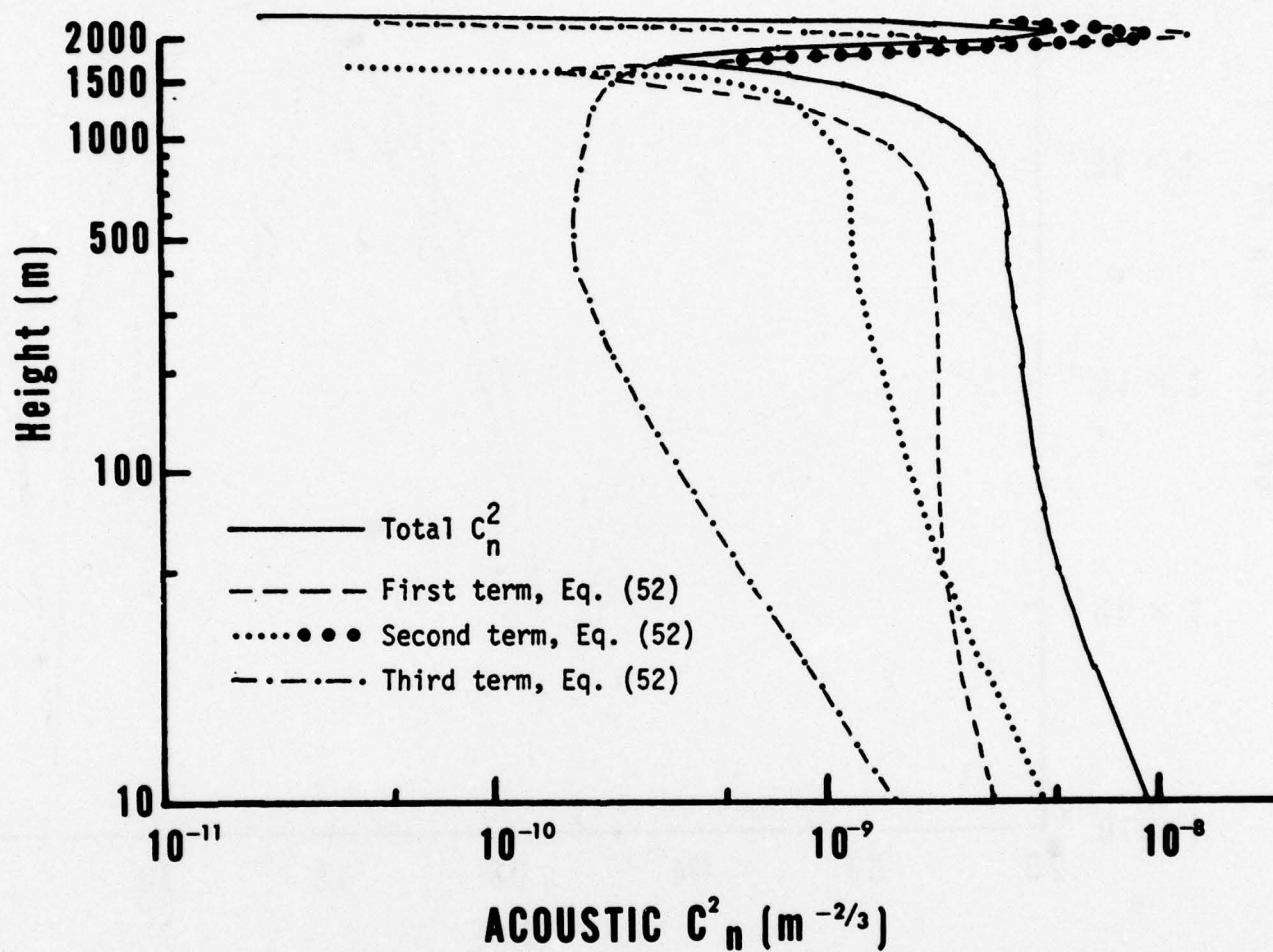


Figure 15. Vertical distribution of terms comprising acoustic  $C_n^2$  at 1800 LT in case C. Heavy dots represent negative values of second term in Eq. (52).

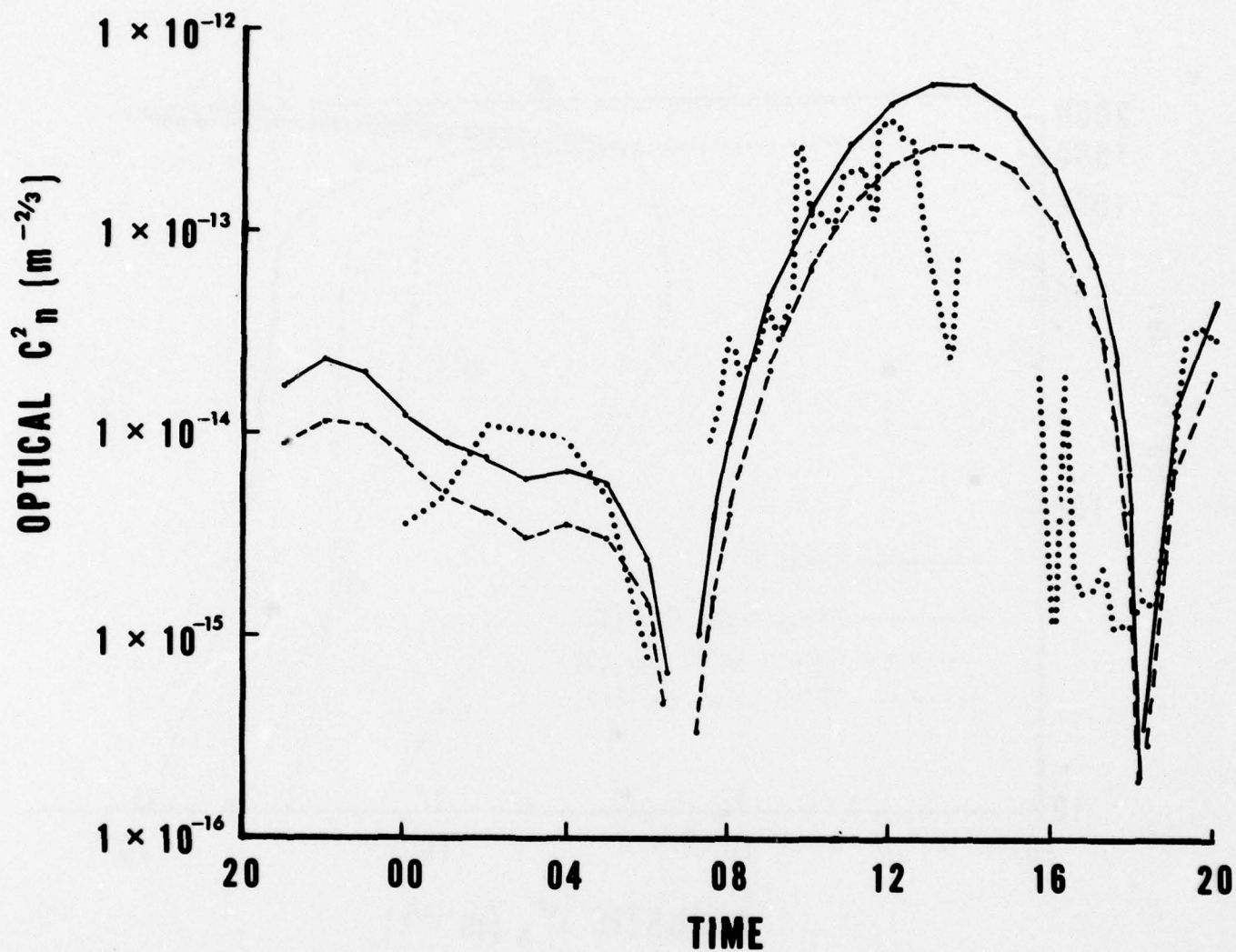


Figure 16. Diurnal variation of optical  $C_n^2$  from model case C and from real data. Dotted line, measured values taken from Wesely and Alcaraz (1973); solid line, model values at 5 m; dashed line, model values at 10 m.